Cappelli, L., Buono, G., Pappalardo, L., van Gerve, T. D., Namur, O., Sielenou, V. N., Ernst, G. G., Mbede, E., Kwelwa, S., Abdallah, E. and Fontijn, K. (2026) “Conduit dynamics of the Rungwe Pumice eruption (Tanzania): From storage to fragmentation of phonolitic-trachytic magmas”, Volcanica, 9(1). doi: 10.30909/vol/bain7754.

Conduit dynamics of the Rungwe Pumice eruption (Tanzania): From storage to fragmentation of phonolitic-trachytic magmas

Lorenzo Cappelli[1], Gianmarco Buono[2], Lucia Pappalardo[2], Thomas D. van Gerve[3], Olivier Namur[3], Vanessa N. Sielenou[1], Evelyne Mbede[4], Shimba Kwelwa[5], Edista Abdallah[4], Gerald G.J. Ernst[6], and Karen Fontijn[1]

[1] Department of Geosciences, Environment and Society; Université libre de Bruxelles; Bruxelles, 1050, Belgium
[2] Istituto Nazionale di Geofisica e Vulcanologia; Italy
[3] Department of Earth and Environmental Sciences, KU Leuven, Leuven, Belgium
[4] School of Mines and Geosciences; University of Dar es Salaam; Dar es Salaam, 35052, Tanzania
[5] AngloGold Ashanti; Geita, 532, Tanzania
[6] Not affiliated

*cappellilorenzo93@gmail.com

ORCiD (LC): 0000-0003-0749-5563
ORCiD (GB): 0000-0002-5474-1985
ORCiD (LP): 0000-0002-3598-587X
ORCiD (TvG): 0000-0002-8776-1552
ORCiD (ON): 0000-0002-9242-0226
ORCiD (EM): 0000-0002-2134-0253
ORCiD (KF): 0000-0001-7218-4513

Keywords: Explosive eruptions; Peralkaline magmatism; East African Rift; Rungwe volcano.

Abstract

The eruptive style of magma is shaped by both storage conditions and ascent processes. Peralkaline melts, with total alkalis exceeding total aluminium, retain relatively high water concentrations and low viscosity and are therefore expected to better resist fragmentation than more common subalkaline melt compositions. However, trachytic and phonolitic magmas can still generate highly explosive eruptions, as demonstrated by the ~4 ka Rungwe Pumice Plinian eruption (Tanzania). This VEI 5 event involved a crystal-poor, microlite-free phonolitic/trachytic magma stored at high temperatures and, in comparison to most peralkaline magmas, with moderate water concentrations. 2D and 3D textural analyses, coupled with embayment speedometry, reveal a delayed homogeneous bubble nucleation event (ΔP_{sat} ~50 MPa) at shallow depths. Rapid bubble nucleation and growth during fast ascent (~6 MPa·s^{-1}) prevented outgassing through a highly vesicular foam and consequently promoted strong melt-gas coupling which, combined with a sudden rheological shift, ultimately led to fragmentation. This eruption underscores the critical role of conduit dynamics in peralkaline magma explosivity, beyond storage conditions alone.

Muhitasari

Mtindo wa mlipuko wa magma huundwa na hali ya uhifadhi na michakato yake ya upandaji. Magma za peralkali zilizoyeyuka, ambazo jumla ya alkali zake inazidi jumla ya aluminiamu, hubakiza ndani yake viwango vya juu vya maji na mnato (viscosity) mdogo, kwa hivyo inatarajiwa kuwa na uwezo wa kustahimili kupasuka vipande vipande zaidi kuliko uyeyukaji wa magma za kawaida za subalkali. Hata hivyo, magma za trakitiki na fonolitiki bado zinaweza kusababisha mlipuko mkubwa sana, kama ilivyoainishwa na mlipuko wa Plinian Pumice wa Rungwe (Tanzania) uliotokea takriban miaka 4,000 iliyopita. Tukio hili lililokuwa na kiwango cha 5 (VEI 5) cha milipuko ya volcano, lilihusisha magma ya fonolitiki/trakitiki isiyo na fuwele (crystals) nyingi wala fuwele ndogo ndogo (microlite), iliyohifadhiwa katika halijoto ya juu sana, ikilinganishwa na magma nyingi za peralkalini, zinazokuwa na kiwango cha wastani cha maji. Uchambuzi wa muundo, kwa kutazama katika pande mbili na pande tatu (2D na 3D), pamoja na upimaji wa kasi ya ghuba (embayment speedometry), unaonyesha uchelewaji katika uundaji wa mfuko wa povu ulio sawa (ΔPsat ~50 MPa) katika kina kifupi. Uundaji na ukuaji wa haraka wa povu (buble nucleation) wakati wa kupanda kwa kasi (~6 MPa·s^{-1}) ulizuia kutolewa kwa gesi kupitia povu lenye vifereji vingi vya hewa ya ndani na hivyo kusababisha muunganiko mkubwa wa magma zilizoyeyuka na gesi, ambao, ulijumuishwa na mabadiliko ya ghafla ya rheolojia, hatimaye ukasababisha kupasuka vipande vipande. Mlipuko huu unasizitiza kuwa uwezo wa kulipuka wa magma za peralkaline hautokani na hali ya uhifadhi pekee bali pia na mienendo ya mipasuko ya miamba.

1. Introduction

Plinian-style explosive eruptions rank among the most severe natural hazards, with impacts ranging from regional to global scales (e.g., Carey and Sigurdsson, 1989; Cioni et al., 2015). These eruptions are governed by a combination of pre-eruptive magmatic conditions—particularly water concentrations and melt composition (e.g., Wilson et al., 1980; Cioni, 2000)—and the dynamic processes occurring within the conduit during magma ascent. Pre-eruptive factors, such as volatile saturation, magma storage depth, and temperature, set the stage for eruption potential by controlling bubble nucleation, crystallisation, and magma rheology (Cashman and Mangan, 1994; Dingwell, 1996; Gonnermann and Manga, 2007; Cassidy et al., 2018). For Plinian eruptions, however, it is within the conduit that magma undergoes a dramatic transformation, from a hot, pressurized silicate melt to a high-energy bubble suspension capable of sustaining explosive fragmentation (Sparks, 1978; Wilson et al., 1980; Cashman and Mangan, 1994).

As magma ascends and decompresses within the conduit, volatile solubility—primarily H_2O and CO_2—decreases significantly, with volatiles eventually reaching saturation. However, because nucleation is energetically demanding, bubbles will form only after a threshold level of volatile supersaturation is exceeded, and this threshold depends on magma properties such as surface tension and volatile diffusivity in the melt (e.g., Mourtada-Bonnefoi and Laporte, 2004; Shea, 2017 among others). When suitable nucleation surfaces are available, such as those of micro- or nanolites inherited from the reservoir or generated during ascent, bubbles can nucleate at relatively lower supersaturation pressures (i.e., the difference between magmastatic pressure at saturation and the pressure at nucleation), resulting in heterogeneous nucleation (Shea, 2017; Cáceres et al., 2022). In contrast, when such surfaces are absent, bubbles nucleate spontaneously through homogeneous nucleation, but only at substantially higher degrees of supersaturation (Mourtada-Bonnefoi and Laporte, 2004; Shea, 2017; Buono et al., 2020). In more exceptional cases, if significant crystallisation occurs at the reservoir level, incipient degassing may initiate magma ascent at greater depths due to second boiling (Edmonds and Woods, 2018).

Following nucleation, bubbles grow by volatile diffusion and decompression and, if exsolved volatiles cannot efficiently escape the system—as commonly occurs in viscous and/or rapidly ascending magmas (e.g., Cassidy et al., 2018)—they drive progressive vesiculation of the melt-gas-crystal mixture (e.g., Sparks, 1978; Proussevitch et al., 1993). This process further accelerates the magma and enhances bubble overpressure, shear stresses and strain rates within the conduit, ultimately promoting magma fragmentation (e.g., Dingwell, 1996; Zhang, 1999).

Understanding the conduit dynamics that dictate the transition between effusive and explosive eruptive style is therefore crucial for predicting eruption explosivity and associated hazards. These dynamics have been extensively studied across a variety of magmatic compositions. For fast-ascending, highly viscous silicic magmas, homogeneous nucleation under high supersaturation conditions is commonly inferred (e.g., Shea, 2017 and references therein), which eventually leads to strain rate-induced brittle failure (Gonnermann, 2015 and references therein). In contrast, for less-viscous basaltic

magmas, heterogeneous nucleation, abrupt rheological changes, or external perturbations (e.g., magma-water interactions) have been suggested to govern eruptive explosivity (e.g., Giordano and Dingwell, 2003; Houghton and Gonnermann, 2008), with ascent rate having a dominant control on preventing outgassing despite high bubble connectivity and permeability (e.g., Houghton et al., 2004; Burgisser et al., 2017; Bamber et al., 2024).

Peralkaline felsic magmas exhibit distinctive physicochemical properties that strongly influence their eruptive behaviour (e.g., Polacci et al., 2004; Shea et al., 2017). With high silica contents ($SiO_2 \geq$ 60 wt.%) and substantial dissolved water (up to 8 wt.% at 200 MPa; e.g., Carroll and Blank, 1997; Di Matteo et al., 2004), these magmas can ascend rapidly within the conduit through density-driven isostatic processes (Browne and Szramek, 2015). Their ascent is further facilitated by viscosities comparatively lower than those of calc-alkaline melts (up to 2-3 orders of magnitude) under comparable T–P–H_2O conditions (Di Genova et al., 2013). This reduced viscosity reflects the high abundance of alkalis and halogens, which weaken the silicate network by breaking Si–O bonds and thus increase the proportion of non-bridging oxygens, producing a depolymerisation effect that is more pronounced than in peraluminous melts (Di Genova et al., 2013). In addition, potentially high dissolved volatile contents, owing to their elevated solubility, further enhance melt depolymerisation. Increased melt depolymerisation enhances volatile diffusivity, facilitating bubble nucleation and growth and thereby reducing supersaturation pressures and bubble overpressures; however, it also promotes vigorous magma foaming, leading to substantial acceleration as vesiculation increases, further favoured by reduced frictional resistance along conduit walls.

Collectively, these conditions can favour efficient outgassing and, potentially, effusive to mildly explosive activity. Yet rapid ascent rates may suppress outgassing efficiency, instead promoting more energetic explosive behaviour, consistent with the widespread occurrence of Sub Plinian to Plinian eruptions of peralkaline felsic magmas (e.g., Pappalardo and Mastrolorenzo, 2012; Hughes et al., 2017; Shea et al., 2017; Pappalardo et al., 2018; Stabile et al., 2021; Wallace et al., 2025). Such explosive events are frequently accompanied by coeval lava effusion, underscoring the need to investigate the eruptive dynamics governing fluctuations in eruptive style within these distinctive magmatic systems (Shea et al., 2017; Andújar and Scaillet, 2012).

Numerical conduit models provide a means to describe and quantify variations in key physical parameters during magma ascent, including pressure, temperature, viscosity, density, ascent velocity, bubble volume fraction, and bubble overpressure within the melt–gas–crystal mixture (e.g., Campagnola et al., 2016; La Spina et al., 2017; Aravena et al., 2018). These parameters ultimately govern magmatic fragmentation and eruptive style. However, the development and calibration of such models require critical constraints that can be obtained from detailed analyses of natural and experimental products of explosive fragmentation, such as pumiceous rocks (e.g., Shea et al., 2010; Campagnola et al., 2016). These products, formed by rapid quenching during fragmentation, preserve in their chemistry and microstructures—particularly vesicularity and crystallinity—a snapshot of the

final conduit conditions immediately prior to fragmentation (Cashman and Mangan 1994; Shea et al., 2010). Their detailed investigation enables the reconstruction of conduit processes, including magma decompression rates, supersaturation pressures, and fragmentation criterion.

Consequently, the methods commonly used to investigate the mechanisms and timescales of magma ascent in volcanic conduits are those based on bubble formation or crystallisation kinetics, as well as on the diffusion of molecules or elements in the melt or in crystals. These approaches rely primarily on the textural and geochemical investigation of eruptive products, respectively (e.g., Costa et al., 2020; Toramaru, 2025). Within this framework, several recent studies have focused on the diffusivity of fast-diffusing volatile elements (such as H and Li) in minerals or melt embayments (i.e., open melt pockets within crystals). In particular, the study of H_2O diffusion in embayments provides an effective way to investigate magma ascent timescale and fragmentation depth (e.g., Costa et al., 2020; Hosseini et al., 2023; Hosseini and Myers, 2024, and references therein). At the same time, textural characterisation of bubbles or microlites (e.g., number density, size distribution, shape and orientation; porosity and permeability) allows the determination of magma ascent rates (e.g., Toramaru, 2006; 2025; Toramaru et al., 2008); additionally, pumice textures provide valuable indicators of several mechanisms such as degassing dynamics, outgassing efficiency, or fragmentation—information otherwise inaccessible—and allow recognition of changes in intra-conduit vesiculation processes that produce distinct pumice types. Such insights are especially important for kinetically reactive magmas like those of peralkaline compositions, where vesiculation and outgassing processes evolve rapidly during ascent (Shea et al., 2017).

This study focuses on conduit processes, highlighting their role in shaping the eruptive behaviour of the Rungwe Pumice (RP) eruption and providing insights into the mechanics of sustained explosive activity of phonolitic-trachytic magmas. The RP eruption offers a unique opportunity to explore the interplay between magmatic dynamics and eruptive processes.

We employ an integrated approach combining traditional 2D textural analysis methods (Cashman and Mangan, 1994; Shea et al., 2010; Gurioli et al., 2015) with advanced 3D imaging techniques using X-ray computed microtomography (μXCT; Polacci et al., 2010; Giachetti et al., 2011; Hughes et al., 2017; Pappalardo et al., 2018, 2023; Valdivia et al., 2022; Buono et al., 2023; Torres-Orozco et al., 2023, 2024). While 2D imaging methods provide valuable insights into vesicle characteristics, they are limited in their ability to represent real textural features and require stereological corrections (Shea et al., 2010). Moreover, 2D analyses cannot fully resolve permeability or vesicle network connectivity (Giachetti et al., 2011). In contrast, μXCT allows for direct, non-destructive 3D observations of these features. However, μXCT accessibility may restrict the number of analysed samples and limit representativity. In complement to these imaging analyses, we utilised embayment water diffusion speedometry (Liu et al., 2007) to cross-check ascent rates estimated from textural data. By combining these techniques, this study aims to provide a comprehensive understanding of the conduit dynamics that sustained the explosive activity of peralkaline phonolitic-trachytic magma during the RP eruption.

2. Geological Background

The Rungwe Volcanic Province (RVP), covering over 1500 km^2, is located in southern Tanzania, within the Western branch of the East African Rift (EAR), and comprises three main Holocene volcanic centres—Rungwe, Ngozi and Kyejo—surrounded by several smaller eruptive centres (**Fig. 1a**; Harkin, 1960; Ebinger et al., 1993; Fontijn et al., 2010a). Volcanic activity in the RVP began at approximately 9 Ma, alternating between effusive and explosive eruptions of high-alkali magmas (Fontijn et al., 2010b, 2012).

Rungwe, the largest volcanic edifice in the RVP, is a relatively young stratovolcano (0.25 ±0.01 Ma, based on whole-rock K-Ar dating on a lava flow at the base of the edifice; Ebinger et al., 1989) centrally located in the province (**Fig. 1b**). It predominantly produced magmas of basaltic, phonolitic, and trachytic compositions. Over its history, Rungwe is estimated to have experienced at least one explosive eruption every 500 years, ranging from violent Strombolian to Plinian events (Fontijn et al., 2010b). Among these, the Rungwe Pumice Plinian eruption stands out as the largest event in the province's Holocene history (Fontijn et al., 2011).

2.1. Rungwe Pumice Eruption

The RP deposit consists of a massive pumice lapilli fall deposit that blankets the entire RVP. Radiocarbon dating and sedimentary records from Lake Masoko place the eruption at ~4000 cal BP (Garcin et al., 2006; Fontijn et al., 2010b). The deposit is lithic-poor and predominantly consists of cream-coloured, highly vesiculated pumice lapilli of high-alkaline, trachytic composition (whole-rock; Fontijn et al., 2013). Alkali feldspar is the primary free mineralogical component, followed by subordinate amounts of biotite, clinopyroxene and Fe-Ti oxides. Notably, cyan-coloured haüyne occurs in the RP deposit, distinguishing it from most other RVP deposits and serving as a field marker for identifying RP outcrops (Fontijn et al., 2011).

The deposit extends on land up to 28 km from the volcano summit, where a 30 cm-thick outcrop has been documented (Fontijn et al., 2011). More distal RP tephra has been recovered from lake sediment cores up to ~115 km SE of Rungwe (Garcin et al., 2006; Fontijn et al., 2011, 2012). On land, outcrops are radially distributed around the summit, and near-circular isopleths indicate wind-still conditions during the eruption (Fontijn et al., 2011). A peak eruptive column height of 30-35 km was inferred using the maximum lithics' size method (Carey and Sparks, 1986; Fontijn et al., 2011), and the absence of associated pyroclastic density current deposits suggests that this column was sustained for most of the eruption. Peak mass discharge rates of 2.8-4.8 $\times 10^8$ kg·s^{-1} were calculated using a range of inferred column heights, and the minimum erupted volume was estimated at 1.4 km^3 dense rock equivalent (Fontijn et al., 2011). Based on these parameters, the eruption was classified as Plinian, with a Volcanic Explosivity Index of 5 (Fontijn et al., 2011), following the classification of Newhall and Self (1982).

A type section for RP deposit was identified at ~11.7 km SSE of the Rungwe summit and designated as KF176 in previous studies (**Fig. 1b**; Fontijn et al., 2010b, 2011, 2013). The section comprises a ~2.5 m-thick, massive pumice lapilli breccia deposit reversely graded at the base and bounded by overlying and underlying palaeosols. The deposit was previously sampled through its entire thickness by Fontijn et al. (2011) and subdivided into 14 samples every 20-25 cm from base to top and labelled sequentially from KF176-B to KF176-O, whereas KF176-A corresponds to the basal palaeosol.

The RP plumbing system has been described as a relatively hot reservoir, ranging from 925 to 975 ±22 °C (Fontijn et al., 2013; Cappelli et al., 2025), of trachytic-phonolitic composition (based on haüyne-hosted melt inclusions major element concentrations). Prior to the eruption, it ponded at shallow crustal depths (at ~3.5 km minimum depth based on saturation pressure models derived from haüyne-hosted melt inclusions; Cappelli et al., 2025) and yielded on average ~4.82 ±0.58 wt.% of dissolved water, while CO_2 was below FTIR detection limit (< 10-100 ppm; Cappelli et al., 2025). The system was likely destabilised by an input of volatile-rich magma, which increased oxygen fugacity, ultimately leading to the eruption (Fontijn et al., 2013; Cappelli et al., 2025).

3. Methods

Samples from the Rungwe Pumice eruption type section KF176 were dry-sieved down to 63 μm and subdivided into granulometric size classes at φ/2 intervals ($\varphi = -\log_2[diameter(\text{mm})]$). To facilitate data interpretation, samples were grouped into five stratigraphic horizons: base (KF176 C-D), bottom half (KF176 E-F-G), middle (KF176 H-I-J), top half (KF176 K-L-M), and top (KF176 N-O). Subsequent analyses kept this partitioning scheme and targeted specific samples as representative of each horizon.

3.1. Embayment diffusivity speedometer

Magma decompression rates were estimated based on the decompression-induced diffusivity-dependent decrease in volatile concentrations within crystal-hosted melt (glass) embayments. Volatile concentration tends to decrease from the innermost portions of embayments to their outlets, which remain in contact with the external melt and undergo re-equilibration of volatile saturation during ascent (e.g., Liu et al., 2007; deGraffenried and Shea, 2021; Geshi et al., 2021; Hosseini et al., 2023).

Accurate inspection of glass embayments was conducted in haüyne crystals, the mineralogical phase hosting the largest number and best-developed melt inclusions among all crystals from the RP eruption (Cappelli et al., 2025). Glass embayments that best preserve volatile concentration gradients tend to exhibit a cylindrical shape, with minimal necking near the outlet and no significant irregularities (deGraffenried and Shea, 2021; Hosseini et al., 2023). They should also lack decompression bubbles in their internal regions while maintaining contact with an external bubble (or its remnant shape) at the outlet (Hosseini et al., 2023). Approximately 25 crystals, handpicked from crushed pumices, were initially selected for measurement. These were collected from the bottom half, middle, top half and top

stratigraphic horizons of the RP deposit. Suitable embayments could not be retrieved from the base of the deposit due to the scarcity of haüyne crystals in this stratigraphic portion.

The crystals were individually embedded in Crystalbond™ thermosetting resin and ground to expose the embayment(s). Afterwards, the resin was melted, and crystals were cast all together in an epoxy resin mount and mechanically polished using diamond pastes down to 1 μm. Water in embayments' glass was analysed with Raman spectroscopy using a Horiba Jobin LabRAM HR Evolution at KU Leuven (Belgium). Samples were irradiated with an Nd-YAG-sourced laser, maintaining low laser power (≤ 50%) to prevent overheating of the resin—particularly in thin embayments—and to avoid potential damage to the crystals. Scattering spectra were acquired in the 150-4000 cm^{-1} wavenumber range and the SilicH2O open-source software (Van Gerve and Namur, 2023) was used to perform the baseline correction and to extract the peak areas. To account for potential interference in cases where embayments were too thin, and noise from underlying phases was recorded, spectra of the host crystal and pristine resin were also acquired and used to correct the glass spectra (Van Gerve and Namur, 2023). Then, water concentrations in the glass were quantified using the calibration feature of SilicH2O. A calibration curve was constructed by correlating the areas of the silica peaks (200–600 cm^{-1} and 800–1300 cm^{-1} ranges) with the area of the water vibrational peak (~3500 cm^{-1}). This calibration was based on spectra of melt inclusions previously analysed by FTIR spectroscopy, for which water contents were independently determined (Cappelli et al., 2025). In total, only nine glass embayments from across the deposit—mostly from its upper portion, where haüyne is more abundant, but also from the middle and bottom half intervals—were successfully measured.

An embayment speedometer was developed by Liu et al. (2007) and subsequently elaborated by several authors using different input parameters and coding languages. In this study, we adopted the publicly available EMBER software, written in MATLAB (Georgeais et al., 2021). EMBER estimates decompression rates by comparing modelled volatile diffusion profiles with the measured concentration gradients in embayments, thereby determining the best fit for decompression rates, initial dissolved concentrations, and initial exsolved gas content. It can determine decompression rates from H_2O, CO_2 and S concentration gradients, however, in our case only water concentrations were available and therefore other volatiles were excluded. Notably, RP glass, both in haüyne-hosted melt inclusions and embayments, was depleted in CO_2, falling below the FTIR detection limit, indicating a minimal effect on water solubility (Cappelli et al., 2025). Input parameters include: i) temperature, assumed constant throughout the ascent and equivalent to RP storage temperature, previously estimated at 975 °C on average (Cappelli et al., 2025); ii) initial pressure, defined as the saturation pressure corresponding to the H_2O concentration plateau in the innermost portions of each embayment, calculated using the trachytic solubility model of Di Matteo et al. (2004); and iii) the final pressure before melt quenching, which was iteratively varied between 0.5 and 25 MPa to achieve the best correlation (minimum squared error). Degassing paths provided as inputs for EMBER were calculated for seven initial exsolved gas contents (between 0 and 3.2 wt.%; see also Georgeais et al., 2021) under closed-system conditions using

VESIcal v1.2.6. (Iacovino et al., 2021) and Thermoengine Python libraries (Ghiorso and Gualda, 2015), both accessible on ENKI servers. A wide range of exsolved gas contents was considered to evaluate any relevant effect on interpolations as in Georgeais et al. (2021), however, as suggested by melt inclusion analyses (Cappelli et al., 2025), a 0 wt.% initial gas was preferred.

Water diffusivity in EMBER is calculated with three different models according to glass composition: basaltic, rhyolitic and intermediate (Georgeais et al., 2021). For the RP composition, we applied the diffusivity model for intermediate compositions using the equations from Ni and Zhang (2018), which are tested for calc-alkaline compositions. We acknowledge that this assumption inevitably introduces some uncertainty; however, diffusivity values calculated under identical conditions using equations more appropriate for trachytic (Fanara et al., 2013) or phonolitic compositions (Fanara et al., 2013; Schmidt et al., 2013) produced results of the same order of magnitude (10^{-10} $m^2 \cdot s^{-1}$). To our knowledge, no published embayment speedometer specifically tested for (per)alkaline magmas currently exists. Decompression rates estimated with EMBER were then compared with textural methods (see §3.4).

Silica content (wt.%), and other major element concentrations, in embayment glasses were measured using a Tescan Mira 4 FEG scanning electron microscope equipped with an Oxford Xplore30 EDX detector at the KU Leuven Core Facility (Belgium). Samples were carbon-coated to a precise thickness of 10 nm, and analysed using an acceleration voltage of 20 keV and a beam current of 6 nA. The Beam Measurement calibration routine integrated into the Oxford Aztec software was used to calibrate Mn elemental concentrations on standard material, ensuring accurate absolute concentrations of major elements. Measurements were performed over areas rather than single spots to minimise the loss of alkali elements, and each embayment was measured 3-10 times to ensure consistency and account for potential variations in glass composition near the embayment outlet. Measurement accuracy was validated by analysing the ATHO-G, StHs6/80-G, and T1-G glass standards (Jochum et al., 2006) multiple times at the start and end of the analytical session. Additionally, glasses of RP crystal-hosted melt inclusions previously analysed with electron probe microanalysis (Cappelli et al., 2025) were used as reference material. For silica concentrations, standards and reference materials yielded a maximum percentage difference to expected values of 0.7% and 0.3% respectively, with a relative standard deviation between measurements of no more than 0.9% (**Supplementary materials**).

3.2. 2D pumice textures

Textures of RP pumice were first evaluated on 2D images of polished sections. Ash particles within the 0/-0.5 φ (1-1.4mm) grain size range from each horizon were rinsed in an ultrasonic bath and then embedded in epoxy resin. A fine grain size range minimises the potential effect of post-fragmentation inflation of gas bubbles that could alter original vesicularity in slower-cooling, larger clasts (Kaminski and Jaupart, 1997; Pappalardo et al., 2018). Moreover, isolated voids in coarser samples often prove difficult to fully impregnate with resin, complicating image processing (Shea et al., 2010). For

comparison, coarse pumice lapilli vesicularity was also investigated by combined gas and water displacement pycnometery (based on Archimedes's principle; methodology and results are presented in **Supplementary Material**). Particles were ground until they were sliced to about half their original volume, then polished with diamond pastes down to 1 μm and finally carbon-coated. Images were acquired in backscattered electron mode (BSE) using an SEC SNE-4500M Plus B scanning electronic microscope equipped with a Bruker EDS Quantax detector at the Laboratoire G-Time of the Université libre de Bruxelles (Belgium). Measurements were performed at an accelerating voltage of 15 keV. For each stratigraphic horizon, one BSE image at x350 magnification was captured for ten randomly selected particles, resulting in a total of 50 analysed particles. The same magnification was used for all particles to ensure representativity—after confirming they yielded similar vesicle size distributions—and to capture larger vesicles while keeping the error for vesicles down to 1 μm equivalent diameter (~22 pixels in area) below 4.5% for a single misrepresented pixel, following the approach of Shea et al. (2010).

Greyscale BSE images were processed using the open-source software Fiji (ImageJ; Schindelin et al., 2012). A preliminary manual rectification was conducted on images to account for vesicles not filled with resin. The Trainable Weka Segmentation tool (Arganda-Carreras et al., 2017) was then applied to classify pumice glass, vesicles and, when present, phenocrysts, producing binary images. Finally, the distance transform watershed algorithm provided in the MorphoLibJ library (Legland et al., 2016) was used to reconstruct vesicle walls lost during sample preparation or due to bubble coalescence during final stage of magmatic ascent.

From the processed binary images, 2D vesicularity (percentage of the area occupied by vesicles), the number of vesicles per unit area (N_a), and the average bubble area were calculated. Each clast was then scored based on the root-sum-of-squares of the variances of these parameters relative to the average value calculated for clasts within the same stratigraphic horizon (i.e., Euclidean distance). The clast bearing the minimum score, representing the least deviation from the average, was identified as the most representative of its stratigraphic horizon and selected for further investigation.

Additional BSE images were collected for these five selected clasts at varying magnifications following the nested image strategy proposed by Shea et al. (2010) for stereological conversion. Specifically, one image was acquired at a magnification sufficient to capture the entire clast (x67-x100), then two images at x350 were taken from areas exhibiting the greatest vesiculation difference based on visual inspection. Within these areas, two images each were captured at x900 (**Fig. 2**). Images were processed in Fiji as previously described. Using FOAM software (Shea et al., 2010), we then obtained statistical descriptors of shapes and sizes of vesicles corrected for magnification choice, cut-effect and intersection probability (Cashman and Mangan, 1994; Shea et al., 2010 and references therein). Stereological conversion in FOAM utilises vesicularity values constrained by three-dimensional reconstructions of particles (§3.3 and 3.4), as vesicularity estimates from the stereological conversion are prone to overestimation (Shea et al., 2010).

3.3. 3D pumice textures

3D maps of pumice clasts were generated using μXCT with a ZEISS Xradia Versa 410 at the Istituto Nazionale di Geofisica e Vulcanologia-Osservatorio Vesuviano (Italy). A single ash particle within the 0/-0.5 φ (1-1.4 mm) grain size range was randomly selected from each of the bottom (KF176-C), bottom half (KF176-F), middle (KF176-I), and top (KF176-O), horizons of the type section. Additionally, a tubular pumice particle (Marti et al., 1999) was selected from the top half horizon (KF176-L) for textural comparison (**Fig. 3**).

The particles were cleaned using an ultrasonic bath before being scanned with μXCT. The field of view was configured to capture nearly the entire volume of each clast, and the working distance was adjusted to maximise resolution. Additionally, a 10x magnification lens was positioned before the detector to optically enhance the resolution, resulting in a final pixel size of 2 μm/px (8 μm^3/voxel). A total of 4001 bidimensional X-ray absorption projections were collected during a 360° rotation of the sample at 80 kV and 7 W. For samples KF176-C, KF176-I, and KF176-O, an additional scan was performed at 150 kV and 10 W decreasing the working distance and using a 20x magnification lens—and consequently reducing the field of view—to obtain an improved resolution of 1.1 μm/px (~1.3 μm^3/voxel). When necessary, a low-energy (LE1) filter was used to minimise beam hardening. The scans were then reconstructed into tomographic volumes using the integrated XRM Reconstructor software.

Tomographic volumes were processed using Dragonfly software (Dragonfly 3D World, 2024). Initially, a U-Net2D super-resolution model (Ronneberger et al., 2015), based on deep-learning neural networks, was trained using correspondent high-resolution (1.1 μm/px) and low-resolution (2 μm/px) volumes and applied to all lower-resolution datasets (2 μm/px). This approach significantly improved these datasets which, due to their larger field of view, captured more extensive and representative volumes of the original particles while maintaining practical scanning times (Buono et al., 2023). The effectiveness of this approach was validated through visual inspection (**Fig. 3**).

Subsequently, glass, vesicles (voids), and phenocrysts were labelled using the U-Net2.5D segmentation model (**Fig. 3**; Ronneberger et al., 2015). For each dataset, the model was trained on at least five 2D areas that had been manually segmented assigning grey-scale values (proportional to phase X-ray absorption) to the corresponding phases. This approach, considering both grey-scale values and shape factors, significantly improves segmentation accuracy, particularly for thin glass walls. Model performance was evaluated by comparing the automated segmentation to manual segmentation, ensuring that a minimum of ~50 two-dimensional patches (64^2 voxels each) per sample were included in the validation set. A maximum binary cross-entropy loss of 0.013 was considered acceptable (average across samples: 0.009 ± 0.002) for the training, while the validation Dice coefficient—computed as 2TP/(2TP+FP+FN), where TP, FP, and FN represent true positives, false positives, and false negatives voxels, respectively—ranged between 0.50 and 0.84. To account for open vesicularity, vesicles open to

the clast exterior were virtually closed at their outlet using a maximum width of 70 μm as a threshold, corresponding to the upper quartile of the volume-weighted distribution of vesicle equivalent diameters. This approach minimized artificial alterations of the vesicle network, avoiding overestimation of naturally open vesicle volumes while retaining a significant portion of the total vesicle volume.

Once glasses and vesicles were segmented, the distance-transformed watershed algorithm was applied to separate individual bubbles that had become connected during the final stages of bubble growth or due to the scanning resolution being insufficient to capture extremely thin glass walls (< 2 μm; **Fig. 3**). This procedure successfully identified most bubbles down to 2 μm (~2 px) in equivalent diameter. Labelled objects smaller than this threshold were excluded from the dataset, to prevent potential noise artefacts (Pappalardo et al., 2018; Liedl et al., 2019; Buono et al., 2020).

3.4. Conduit dynamic modelling

From the textural datasets, we retrieved several parameters that were used as inputs for models or as quantitative descriptors of conduit dynamics. Pumice vesicularity (ϕ) was defined as the percentage of volume occupied by vesicles relative to the total volume (i.e., voids + glass – phenocrysts), while vesicle connectivity as the percentage of a connected vesicle network (pre-watershed, see §3.3) relative to the total vesicle volume. Volumetric descriptors of the shape and size of each vesicle (post-watershed) were used to construct vesicle size distribution and vesicle population density trends that can be used to describe the nucleation process (Cashman and Mangan, 1994; Shea et al., 2010 and references therein). Vesicle number density (VND), a key parameter for estimating magma decompression rates from vesicle textures (e.g., Toramaru, 2006; Shea, 2017), was calculated by dividing the total number of vesicles (post-watershed) by the glass volume (Proussevitch et al., 2007). Decompression rates were computed using the model developed by Toramaru (2006) in its simplified version proposed by Shea (2017)

$$\frac{dP}{dt} = \left(\frac{N_V}{A \times 10^4}\right)^{\frac{2}{3}} \quad (1)$$

where N_V corresponds to VND (mm^{-3}) and A is a composition-dependent fitting constant (3 ± 1.8 for phonolites and trachytes; Shea, 2017).

3.4.1. Supersaturation pressure

The supersaturation pressure of bubble nucleation (ΔP_{sat}), and the related nucleation pressure (P_n), were estimated for a given decompression rate by integrating nucleation rates for progressive decompression steps (t_i in Eq. (3) in Mourtada-Bonnefoi and Laporte, 2004) and iteratively recalculating the bubble number density (Eq. (4) in Mourtada-Bonnefoi and Laporte, 2004) until the latter overpassed the value of 1 mm^{-3} (Mourtada-Bonnefoi and Laporte, 2004; Shea, 2017). The

nucleation rate of bubbles (J) at a given melt pressure (P_M) was calculated following the classical nucleation theory (Hirth et al., 1970; Shea, 2017):

$$J = \frac{2n_0^2 DV}{a_0} \cdot \sqrt{\frac{\sigma}{kT}} \cdot exp\left(-\frac{16\pi\sigma^3}{3kT(P_B - P_M)^2}\theta\right) \quad (2)$$

where θ is a geometric factor equivalent to 1 or $0 < \theta < 1$ for homogeneous and heterogeneous nucleation respectively (Shea, 2017), and k is the Boltzmann constant (i.e., 1.38×10^{-23} $m^2 \cdot kg \cdot s^{-2} \cdot K^{-1}$). T (K) is the temperature of the melt at the reservoir conditions (1248 ± 22 K; Cappelli et al., 2025). The water saturation pressure, P_{SAT} (Pa), was set to 92 ± 15 MPa, determined using saturation models in crystal-hosted melt inclusions (see Cappelli et al., 2025 for a detailed definition of the pressure parameter), and used to calculate P_B (Pa) which is the internal pressure of an incipient bubble nucleus, iteratively calculated for each step of P_M (Shea, 2017; Buono et al., 2020). D ($m^2 \cdot s^{-1}$) is the diffusivity of the volatile phase in the melt, calculated for water in phonolitic and trachytic melts using the model of Fanara et al. (2013). The volume of volatile molecules V (m^{-3}) was calculated according to Eq. (5) in Shea (2017). The mean distance between volatile molecules in the melt, a_0 (m), was derived as $n_0^{-1/3}$, where n_0 ($mol \cdot m^{-3}$) represents the number density of volatile molecules. n_0 was determined using Eq. (6) in Shea (2017) with inputs derived from haüyne-hosted melt inclusion data (Cappelli et al., 2025) which provided initial dissolved water concentrations (i.e., 4.82 ± 0.58 wt.% on average, converted to a single-oxygen mass fraction) and melt density (2250 ± 10 $kg \cdot m^{-3}$ on average). Finally, σ ($N \cdot m^{-1}$) corresponds to the surface tension that can be either calculated for homogeneous nucleation adopting the Eq. (13) from Shea (2017) or fixed at the average value of 0.025 $N \cdot m^{-1}$, considering magnetite microlites as primary nucleation sites (Shea, 2017). A Monte Carlo simulation with 5000 iterations was run separately for homogeneous and heterogeneous nucleation to assess the statistical representativeness of ΔP_{sat} and P_n and to quantify their uncertainty. For each iteration, random values of T, P_{SAT}, X_{H2O}, X_{SiO2}, ρ, and dP/dt were sampled from normal distributions defined by their measured means and standard deviations, then ΔP_{sat} was calculated accordingly. For heterogeneous nucleation, the wetting angle was additionally sampled from the range appropriate for Fe–Ti oxides (i.e., 90º-160º), which are the mineral phases most effective at promoting bubble nucleation (e.g., Shea, 2017).

3.4.2. Volatile outgassing in a porous magma

Tortuosity measures the deviation of the flow path between two bubbles from a straight line along the flow direction. It is a critical parameter reflecting the roughness of a porous medium and is therefore directly related to its permeability. However, due to the highly intricate network of vesicles, it was computationally impractical to quantify tortuosity directly using Dragonfly's skeletonization on a volume sufficiently large to be representative of the datasets. As an alternative, we utilized the tortuosity factor (τ^*), which quantifies the difference between diffusivity under laminar conditions (fully conductive) and the actual diffusivity through the porous medium (Epstein, 1989; Cooper et al., 2016).

Tortuosity factor can be related to tortuosity through Archie's law (Eq. (4) in Degruyter et al., 2012). To calculate τ^*, we used the MATLAB application *TauFactor*, which computes τ^* along three mutually perpendicular directions on cuboid volumes (Cooper et al., 2016). These cuboids were extracted from labelled vesicle volumes (pre-watershed), selecting the largest possible cuboid for each dataset, always ensuring it was several orders of magnitude larger than the largest vesicle present in the dataset (Pappalardo et al., 2018). When present (§**4.1**), the preferential orientation of vesicles, indicated by the direction of their equivalent ellipsoid major axes, was used as a proxy for the primary flow direction, and the y-axis of each cuboid was oriented accordingly.

Darcian permeability (m^2) across the above-mentioned cuboid volumes was calculated using the Kozeny-Carman relation (Rust and Cashman, 2004; Degruyter et al., 2012; Wei et al., 2018; Valdivia et al., 2022) along each of the three perpendicular directions:

$$k_D = \frac{\varphi^3}{cS^2\tau^2} \quad (3)$$

where the square of tortuosity is calculated through Archie's law, φ is vesicularity, S (m^{-1}) is the surface area per unit volume of the vesicle network and c is the Kozeny constant for pores-controlled media (set to 8; Degruyter et al., 2012).

Key parameters describing the flow of volatiles through porous media (outgassing) and their coupling with magma ascent include the dimensionless Forchheimer (*Fo*) and Stokes (*St*) numbers (Rust and Cashman, 2004; Degruyter et al., 2012; Zhou et al., 2019; Valdivia et al., 2022 and references therein). The Forchheimer number is defined as the ratio between the inertial and viscous forces resisting the flow. Similar to Reynolds number, it characterises flow behaviour, with lower *Fo* values indicating laminar flow. It can be expressed as (Rust and Cashman, 2004; Degruyter et al., 2012 and references therein):

$$Fo = \frac{\rho_g v}{\mu_g} \cdot \frac{k_D}{k_I} \quad (4)$$

where ρ_g is the density of the volatile phase defined as $P_M/(RT)$ with R as the specific gas constant for water (461.4 $J \cdot kg^{-1} \cdot K^{-1}$; Degruyter et al., 2012) and P_M the pressure in the conduit at a given depth, iterated during decompression; μ_g is the viscosity of the volatile phase (15×10^{-5} Pa·s; Degruyter et al., 2012); v ($m \cdot s^{-1}$) is the average magma ascent velocity, calculated as the ratio of the mean decompression rate to the magmastatic gradient in the conduit (approximated by the lithostatic gradient, 0.027 $MPa \cdot m^{-1}$; Browne and Szramek, 2015); and k_I is the inertial permeability (Rust and Cashman, 2004; Zhou et al., 2019) derived from k_D using the relationship proposed by Gonnerman et al., (2017; Eq. (B1)).

The Stokes number is defined by the ratio of the response time of magma to the flow time of volatile phases (Degruyter et al., 2012) and at low values indicates strong coupling between volatiles and the ascending magma. *St* can be expressed as (Degruyter et al., 2012):

$$St = \frac{\frac{\rho_B k_D}{\mu_g}}{\frac{r}{\overline{v}}} \quad (5)$$

where ρ_B (kg·m^{-3}) is the bulk density (melt + bubbles) and r is the radius of the conduit estimated from eruption mass discharge rate (§5.1).

4. Results

4.1. Vesicularity and vesicle metrics

Vesicularities determined from three-dimensional imaging ($\overline{x}$ ~63% ±5%) are, on average, lower than values obtained using 2D analyses ($\overline{x}$ ~74% ±6%). However, both 2D and 3D datasets yield consistent vesicularities when comparing samples within or across different stratigraphic horizons (**Table 1**). Despite this discrepancy between 2D and 3D datasets, the consistent values of vesicularity and VND in pumiceous ash (%RSD ~7%) observed from 2D imaging across a wide selection of clasts confirms that randomly selected single clasts were sufficiently representative for μXCT analysis. Connected vesicle networks consistently account for 99.9% of the total vesicularity.

Vesicularity estimated from 3D reconstructions is influenced by the selection of grey-scale threshold during segmentation; however, conservative manual segmentation demonstrates that this effect on total vesicularity is minimal (~5 vol%) and deep learning models effectively delineate vesicle contours, preserving even the thinnest vesicle walls detectable at the applied resolution. The method's reliability is further supported by the small differences (5-8%) between scans collected at 20x and 10x (improved with the super-resolution model) magnifications, confirming the robustness of the approach despite a slight tendency to underestimate vesicularity at the lower resolution. The discrepancy between 2D and 3D analyses thus likely arises from the limitations of bidimensional sectioning and sample preparation (e.g., glass breakage), which struggles to accurately represent irregular vesicles, risking overestimation of vesicularity (Shea et al., 2010). Vesicularity of lapilli-sized clasts analysed with pycnometry methods ranges around 0.85 ±0.04 (**Supplementary Material**). This high degree of vesicularity may result from post-depositional bubble inflation, which is more likely in larger clasts due to prolonged cooling times (Thomas et al., 1994; Kaminski and Jaupart, 1997). This phenomenon is visually evident from the occurrence of millimetric to centimetric vesicles on clast surfaces, which can influence and potentially alter original vesicularity determinations (**Supplementary Material**).

VNDs derived from both 2D and 3D imaging datasets yield values on the order of (10^{14} m^{-3}), and are again consistent across different stratigraphic horizons. VND values from both datasets are reported in **Table 1**. In 3D reconstructed particles, vesicle volume distributions (VVDs) predominantly exhibit lognormal distributions, with unimodal modes—indicating the volumetrically most represented size—ranging from 28 μm (log(L) = - 1.55) to 57 μm (log(L) = -1.25) equivalent diameters (**Fig. 4; Table 2**). Vesicle size distributions (VSDs) exhibit curved trends with one or more break points and tend to level

off at larger sizes (**Fig. 5**). Such distributions are strongly influenced by the choice of bins, which, in this case, are linearly spaced and equivalent in number to the geometric binning used for VVDs (Shea et al., 2010). Artefact spikes or broken segments may appear as a result. However, VSD trends of the finest vesicles allow us to extrapolate angular coefficients and intercepts at L = 0 mm (**Fig. 5**; **Table 2**), which are useful for estimating vesicle growth at late nucleation and growth conditions (§5.2). Cumulative vesicle size distributions (CVSDs) follow exponential trends but exhibit slope breaks at the largest sizes (**Supplementary Material**). These may reflect difficulties in accurately representing the largest vesicles, potentially due to the effects of bubble coalescence (e.g., Blower et al., 2002; Pappalardo et al., 2018; Liedl et al., 2019). Size distribution descriptors derived from the stereological conversion of 2D textures are consistent with those obtained from 3D reconstructions (**Fig. 6; Supplementary Material**).

In 2D sections, vesicles are generally subrounded; however, larger vesicles tend to deform and flatten at contacts with neighbouring vesicles or adopt irregular polylobate shapes especially when coalesced (**Fig. 2**). The average vesicle sphericity of 3D datasets ranges between 0.64 and 0.74 with a narrow spread ($\pm 0.09 < 1\sigma < \pm 0.12$). Sphericity is also negatively correlated with vesicle size (equivalent sphere diameter), and larger vesicles tends to be more irregular (**Supplementary Material; Table 2**). While no significant differences are observed across the other horizons, the minimum sphericity value is observed in the tube pumice, where vesicles predominantly exhibit elongated shapes. The preferential orientation of vesicles is evident in pole figures representing the orientation density of the vesicle's major axis relative to three mutually perpendicular axes (**Supplementary Material**). Although most pronounced in tube pumice, other samples also show a mild preferential orientation.

4.2. dP/dt and ΔP_{sat}

Estimates of 3D VND-based decompression rates (Shea, 2017) are consistent across stratigraphic horizons, ranging between 4.8 and 7 MPa·s^{-1}, with an average of 5.9 ± 2.4 MPa·s^{-1}. The relatively large uncertainty partly reflects propagation of the ~40% relative error associated with the compositional constant *A* in Eq. (1). In contrast, when model uncertainty is excluded, the average decompression rate across all samples yield a narrower $\pm 1\sigma$ of 0.9 MPa·s^{-1}, with the tube pumice being the only outlier, recording a comparatively lower value of 2.8 MPa·s^{-1} (**Table 3**). These values fall within the same order of magnitude—though slightly lower—than those obtained from stereologically converted 2D VND, which yield an average of 7.5 ± 3 MPa·s^{-1}. Decompression rates obtained using the embayment speedometer were evaluated across a range of initial dissolved water contents and final quenching pressures, according to the minimum least error (Georgeais et al., 2021). The resulting rates are generally of the same order of magnitude as those derived from vesicle texture analyses ($\overline{x} = 1.74 \pm 0.75$ MPa·s^{-1}; **Table 3; Fig. 7**). An initial dissolved water content of ~4.3 wt.% consistently provided the best fits, falling within the uncertainty range of initial water contents inferred from melt inclusions (4.82

± 0.58 wt.%; Cappelli et al., 2025), with final quenching pressures ranging around 13 ± 6 MPa (**Supplementary Table 1**).

The Monte Carlo simulation for homogeneous nucleation yields a median ΔP_{sat} of ~52 MPa (with a 16th–84th percentile range of 51–55 MPa) corresponding to an average nucleation pressure of ~40 MPa. Under a heterogeneous nucleation regime, the simulation produces a substantially lower ΔP_{sat} of ~16 MPa (16th–84th percentile range of 17-18 MPa), and an average Pn of ~76 MPa, primarily due to the reduced surface tension (σ in **Eq. 2**). Detailed simulation outputs are provided in **Supplementary Materials**.

4.3. Volatile outgassing

The tortuosity factor for "standard" clasts ranges from 1.70 to 3.78 and is consistent for the three directions investigated ($\pm 1\sigma$ = 0.12 to 0.72). In contrast, the tube pumice exhibits much greater heterogeneity, with a relative standard deviation of 50% between the directions orthogonal to the major elongation of vesicles and the one parallel to it. A similar observation comes from Darcian permeability of clasts, which overall ranges from 1.27×10^{-13} and 1.27×10^{-12} m^2, and between 1.18×10^{-14} and 7.48×10^{-13} m^2 for the tube pumice, showing a relative standard deviation of 125% (**Table 3**).

Stokes and Forchheimer numbers are calculated using the average of Darcian permeability across each direction, except for the tube pumice where the maximum value was used to account for its anisotropy. For the other samples, Stokes numbers range from 2.44×10^{-5} and 1.44×10^{-4} (**Table 3**), indicating significant gas-melt coupling (**Fig. 8**; Rust and Cashman, 2004; Degruyter et al., 2012). Forchheimer number calculations were iterated between the lowest estimated nucleation pressure (40 MPa) and a minimum quenching pressure of 13 MPa (§5.2), and consistently exceeded a value of 10^4, suggesting a predominantly turbulent and hindered flow of volatiles through magma vesicularity (Degruyter et al. 2012).

5. Discussion

5.1. Sustained activity during the RP eruption

Plinian-style eruptions are characterised by the violent ejection of pyroclastic materials and could last for hours or even days, potentially maintaining a quasi-stable mass discharge rate (MDR; Cioni et al., 2015 and references therein). Changes in MDR during a prolonged eruption may occur due to factors such as reservoir replenishment, conduit widening, or variations in volatile concentrations (e.g., Carey and Sigurdsson, 1989). MDR fluctuations can be identified at the outcrop scale—where they may manifest as grading in fallout deposits or the onset of pyroclastic fountaining, which generates pyroclastic density currents—but are also preserved in textures of pumiceous products.

The pyroclastic fall deposit of the RP eruption is reversely graded at the base, suggesting an initial intensification of eruptive explosivity (Fontijn et al., 2011). Above this interval, the deposit remains

590 massive to the top and lacks evidence of widespread PDCs descending the volcano's flanks. This stratigraphy suggests sustained eruptive activity throughout the event (Fontijn et al., 2011), although we cannot exclude that poorly preserved or unidentified small PDCs may have been deposited close to the volcano summit (within a travel distance of 1-2 km; Fontijn et al., 2011). To evaluate whether these stable eruption conditions are also reflected in steady decompression rates and dynamics of bubble
595 nucleation and growth, we analysed eruptive products collected from different horizons of the deposit, spanning its vertical extent.

VND, vesicularity, inferred magma decompression rate and outgassing parameters all remain within the same order of magnitude across the deposit, and each horizon yields average z-scores within 1σ (**Table 3**; **Fig. 9**). The consistency of these conduit parameters suggests that bubble evolution and
600 fragmentation mechanisms remained largely unaltered throughout the RP eruption. One exception is the central horizon, represented by sample KF176I. This sample displays the highest VND—and thus the highest inferred decompression rate—yielding a greater proportion of smaller vesicles relative to the other samples (**Fig. 5**). It also produces the highest explosivity score, calculated as the average of min–max normalised values of interdependent explosivity indicators (decompression rate and Darcian
605 permeability; **Fig. 9**). This modest deviation may reflect either a brief peak in ascent rate or, more plausibly, natural variability within the magmatic foam.

By inverting Eq. (16) for MDR from Shea (2017), we estimated conduit radius (assuming a cylindrical conduit) as a function of magma bulk density—derived from glass density and pumice vesicularity—and decompression rate. Using a representative value from the peak MDR range reported
610 by Fontijn et al. (2011) (i.e., 3.8×10^8 kg·s^{-1}), based on maximum column-height estimates, we calculated a conduit radius for each stratigraphic horizon, yielding a skewed distribution with an average of 28 ± 3 m (**Table 3**). These values are systematically smaller than previous crater radius estimates of 50–60 m (Fontijn et al., 2011), which instead possibly represent shallower vent conditions (Woods, 1998), above the magma fragmentation level, where erosion process in the conduit wall
615 reaches maximum efficiency (e.g., Macedonio et al., 1994). Given the stable decompression rates independently inferred throughout the sequence, we find no evidence for progressive conduit widening when assuming a constant peak MDR. Conduit widening during sustained Plinian eruption is considered a common process, as conduit erosion can increase conduit width by several meters over timescales of hours (e.g., Carey and Sigurdsson, 1989; Cioni et al., 2015). Under a constant peak MDR,
620 such a few-meter radius increase would reduce decompression rate only slightly (< 1 MPa·s^{-1}). Although we do not observe this trend, a small widening of a few meters may fall within the uncertainty of our estimates (±1σ ≈ 3 m) and therefore remain unresolved. In contrast, if MDR had progressively increased toward a peak—though not supported by field data—then, for a constant decompression rate, the conduit would need to widen substantially during the eruption, as a twofold increase in MDR would
625 enlarge the radius by ~10 m.

The 3D textures of vesicles in the tube pumice show slightly lower VND, though still within the same order of magnitude, and surface area per unit volume, resulting in an estimated decompression rate approximately half that of the "standard" ash samples. The tube pumice sample also displays the strongest iso-orientation of vesicles (**Fig. 10**; **Supplementary Material**), which are predominantly larger in size, along with the highest variability in permeability and outgassing efficiency across the three investigated directions (**Table 3**). These characteristics are associated with high shear conditions occurring along the conduit walls, where friction with the bedrock is maximal and promotes elongated bubble channels, particularly at high ascent rates (Marti et al., 1999; Mastin, 2005; Torres-Orozco et al., 2023). However, these frictional forces also act to slow the ascent, generating a radial gradient in ascent velocity, explaining the lower estimated decompression rate (Gonnermann and Manga, 2003). As tube pumices are found throughout all horizons (on average 5 ±2% of components; Fontijn et al., 2011; Cappelli et al., 2025), they are interpreted as a product of localised enhanced shear stresses rather than evidence of changing ascent conditions.

5.2. Bubble nucleation and growth dynamics

The absence of microlites and the very low phenocrysts abundance (≤ 0.03 vol.%) suggest that the bubble nucleation in the RP magma was most likely dominated by homogeneous processes. Iron-titanium oxide nanolites, which would be below the spatial resolution of the μXCT datasets, could in principle act as heterogeneous nucleation sites (Shea, 2017; Cáceres et al., 2022). However, no nanolites were observed even at the highest magnification during SEM imaging (0.04 μm·pixel^{-1}), nor was the diagnostic Raman peak at ~690 cm^{-1} associated with Fe-bearing nanolites (Di Genova et al., 2017) detected at embayment outlets, where melt is in direct contact with the external bubble and water loss—and thus nanolite formation—would be expected to be most pronounced. Although the presence of undetected nanolites cannot be entirely excluded, there is no evidence that such phases formed prior to, or triggered, the onset of significant bubble nucleation. Instead, nanolite crystallisation, if present, may be promoted by melt dehydration following bubble formation, rather than preceding it. In addition, heterogeneous nucleation may also be favoured by structural heterogeneities in the melt inherited from reservoir conditions (Shea, 2017 and references therein). However, the relatively low viscosity of hot, hydrated phonolitic melts likely facilitates rapid structural relaxation and chemical homogenisation thanks to higher element diffusivity, reducing the persistence of melt heterogeneities compared to more polymerised silicic melts. This behaviour would tend to shift nucleation towards more homogeneous conditions, even though complete structural homogenisation is challenging in natural systems lacking prolonged superliquidus annealing (Shea, 2017). Therefore, while minor heterogeneous nucleation cannot be ruled out, the available textural, spectroscopic, and compositional evidence supports homogeneous nucleation as the predominant mechanism in the RP magma, occurring relatively late during ascent in the conduit under conditions of higher supersaturation pressure and shallow depths, following chamber rupture and initial dyke propagation driven by magmatic overpressure and buoyancy

forces (e.g., Browning et al., 2015). Such conditions were likely promoted by the input of a volatile-rich magma from depth (Fontijn et al., 2013; Cappelli et al., 2025).

Ascent velocity of magma in the conduit is a pivotal factor influencing processes ranging from bubble nucleation to outgassing efficiency (e.g., Gonnermann and Manga, 2007; Cassidy et al., 2018 and references therein). Decompression rates derived from the VND-based model (5.9 ±2.4 $MPa \cdot s^{-1}$) align with values reported for violent explosive Plinian-style eruptions of similar compositions (e.g., Vesuvius 79CE; Campanian Ignimbrite, Campi Flegrei; Pomici di Base, Somma-Vesuvius; Green Tuff, Pantelleria; Baricha ~87 ka; Campagnola et al., 2016; Shea, 2017; Cassidy et al., 2018; Pappalardo et al., 2018; Tadesse et al., 2024; **Fig. 7**). The VNDs used here—on the order of 10^{14} m^{-3}—fall within the typical range for Plinian deposits (e.g., Humphreys et al., 2008; Rust and Cashman, 2011; Shea, 2017; Buono et al., 2020 and references therein). However, we note that the automated watershed algorithm may underestimate VND by failing to fully reconnect bubble walls lost during coalescence; however, even doubling the number of bubbles would not shift the order of magnitude of either VND or the resulting decompression rates. This methodological limitation therefore has minimal influence on our estimates, particularly given the consistency with 2D datasets. These VND-derived values probably represent peak decompression rates (Shea, 2017), occurring during the late conduit acceleration when bubble expansion is most vigorous until fragmentation and quenching, preserving in pumice textures a maximal VND.

Embayment speedometers, in contrast, cannot record the highest decompression rates because during the final acceleration stage the timescale of H_2O exsolution can become too short for concentration gradients to track the pressure drop (Humphreys et al., 2008; Hosseini et al., 2023). Experiments demonstrate that above ~0.25 $MPa \cdot s^{-1}$ equilibrium degassing cannot be maintained (Gardner et al., 1999), promoting H_2O supersaturation and potentially leading to overestimation of decompression rates inferred from embayment profiles (Humphreys et al., 2008). Our embayment-derived values (1.74 ± 0.95 $MPa \cdot s^{-1}$) are lower than the VND-based rates, and fall within the upper range of values reported so far in the relatively few studies using similar models (e.g., up to 1.6 $MPa \cdot s^{-1}$; Shea, 2017; Hosseini et al., 2023). These values are either similar (e.g., 0.9–1.6 $MPa \cdot s^{-1}$ for the 1980 Mount St. Helens eruption; Humphreys et al., 2008) or higher (e.g., 0.008–0.25 $MPa \cdot s^{-1}$ for the 3.6 ka Santorini eruption; Myers et al., 2021) than values previously reported for other Plinian eruptions. Such variations may result from the natural variability of Plinian eruptions or from the lack of standardised procedures for determining decompression rates using this method. Four our estimates, this difference may reflect our choice of starting conditions in EMBER, in particular allowing initial H_2O contents to vary around the observed embayment plateau concentrations rather than fixing them to melt inclusion-derived values and, accordingly, setting initial pressure equal to the saturation pressure of the plateau concentrations. Such assumptions have been shown to yield decompression rates up to 20 times higher than previous estimates (Georgeais et al., 2021) and are consistent with the expectation that ascent rates are not constant. For example, an initial slow, near-equilibrium ascent stage may allow embayments to

re-equilibrate in their innermost portions and allow a diffusion gradient to start forming at pressures lower than reservoirs. Such multistep decompression paths have been invoked to reconcile discrepancies among different speedometers—VND, microlite, and embayments—within single eruptions (e.g., Harris et al., 2024).

Because the quenching plateau pressures (84 ± 16 MPa) overlap within uncertainty of melt inclusion–derived saturation pressures (92 ± 15 MPa), a prolonged initial slow-ascent phase is unlikely or negligible. Therefore, embayment-derived values are interpreted to record an average, conduit-scale decompression rate, whereas VND–based rates capture the final and fastest decompression pulse approaching fragmentation, when the magma reaches peak acceleration. Assuming a constant magmastatic gradient equivalent to the average lithostatic gradient (0.027 $MPa \cdot m^{-1}$), the peak decompression rate implies a maximum apparent ascent velocity of 218 $m \cdot s^{-1}$ at fragmentation. Such high velocities are consistent with gas–magma mixture exit velocities at the vent, as inferred from explosive eruption modelling (e.g., Degruyter et al., 2012; Cassidy et al., 2018). However, decompression rates inferred at fragmentation correspond to transient, local pressure release at the fragmentation front and cannot be directly interpreted as bulk magma ascent velocities. Instead, these values likely reflect near-vent outlet conditions dominated by rapid gas expansion, permeability increase, and shear-induced pressure relaxation, rather than vertical magma movement (e.g., Gonnerman 2015). In contrast, the average decompression rate derived from embayment speedometry (e.g., 1.74 $MPa \cdot s^{-1}$) yields an ascent velocity of ~64 $m \cdot s^{-1}$ which is more representative of conduit-scale magma transport. Such rapid ascent can suppress microlite crystallisation, favouring homogeneous nucleation during ascent.

We estimated a homogeneous supersaturation pressure for bubble nucleation of approximately 52 MPa, based on an initial reservoir pressure of 92 MPa, which corresponds to a nucleation pressure of 40 MPa. This significantly limits the time available for nucleation and growth. Decompression experiments demonstrated that a supersaturation pressure of ~50 MPa is sufficient to trigger homogeneous nucleation in evolved alkaline melts, as opposed to much higher ΔP_{sat} required in rhyolitic subalkaline or calcalkaline melts (100-180 MPa; Shea, 2017; Buono et al., 2020). In alkaline melts, the bubble number density peak (i.e., VND final order of magnitude) is almost reached within the first nucleation event at $\Delta P_{sat} \leq 50$MPa (Mourtada-Bonnefoi and Laporte, 2004; Buono et al., 2020). Further decompression may increase the VND by 1-2 orders of magnitude through multiple or continuous nucleation events (Mourtada-Bonnefoi and Laporte, 2004; Gonnermann and Manga, 2007; Buono et al., 2020), which coupled with bubble growth, eventually culminates in bubble coalescence and fragmentation.

The available time for bubble growth is therefore constrained between the nucleation depth (~1.9 km equivalent to a magmastatic pressure of 40 MPa) and the fragmentation level. In principle, water concentrations measured at the embayment mouths should reflect the final water saturation state of the melt prior to quenching and thus provide an estimate of the fragmentation depth. However, surface

irregularities at the rims of polished glass embayments limited Raman measurements to a few micrometres inward from the embayment mouths, As a result, saturation pressures derived from these measurements (30 ± 7 MPa on average; **Supplementary Material**) are interpreted as maximum estimates of fragmentation pressure. An alternative constraint is obtained by extrapolating the best-fitting decompression path modelled to zero distance in water concentration profiles. This approach yields an average final quenching pressure of 13 ± 6 MPa, implying a relatively short interval for bubble growth. Given that nucleation initiated near 40 MPa, this corresponds to 8–42 s, assuming an average decompression rate of 1.74 ± 0.95 MPa·s^{-1}.

Nevertheless, the differing timescales of decompression and volatile diffusion suggest that complete re-equilibration was unlikely. Over the inferred decompression interval, only the outer 4-10 μm within embayments would have enough time to re-equilibrate by diffusion (using $t = L^2/2D$; Buono et al., 2020, with D from Fanara et al., 2013), given the minimum residual ~1.3 wt.% H_2O observed at embayment mouths. Consequently, the melt likely remained supersaturated in H_2O and, also considering EMBER is calibrated for comparatively water-poorer calc-alkaline melts, the quenching pressure estimate may overestimate the fragmentation depth, implying that fragmentation could have occurred at slightly shallower levels.

VSDs and VVDs indicate continuous nucleation and growth under disequilibrium degassing conditions (Cashman and Mangan, 1994; Klug and Cashman, 1994; Blower et al., 2001, 2002; Shea et al., 2010), with minor bubble coalescence effects that flatten the VSD curves in the larger size regions, particularly evident in bottom half horizon (**Fig. 5**). The small equivalent diameter of the modes (39 ± 6 μm) indicates a fine vesicularity (**Table 2**), consistent with the estimated limited time available for bubble growth. Using the time for bubble nucleation and growth (t), calculated assuming a constant decompression rate between 40 and 13 MPa, a minimum average growth rate (G) of ~7 ×10^{-4} mm·s^{-1} was estimated via the relation $a = -1/Gt$, where a is the angular coefficient of higher VSD trends (**Fig. 5**; Cashman and Mangan, 1994; Klug and Cashman, 1994; Klug et al., 2002). Peaks in bubble growth rates have been modelled at up to 0.1 mm·s^{-1} for rhyolitic melts (Proussevitch and Sahagian, 1998). In contrast, the lower growth rates modelled for the RP suggest that bubble nucleation dominated over bubble growth even during the last stages of ascent. The exponential form of CVSDs further supports continuous bubble nucleation during ascent, driven by decompression-induced disequilibrium (Blower et al., 2001, 2002). However, as these CVSDs are not able to develop a full power-law trend, it implies a limited number of nucleation events (< 5; Blower et al., 2001), likely due to insufficient time or diffusion-limited processes to allow formation of new bubbles to fill void spaces within growing ones in the final ascent stages. This suggests that VND was rapidly established mainly during early nucleation events of bubbles, which had limited time to grow. As bubbles came into contact with each other, they began to coalesce resulting in a poorly organised packing of approximately equally sized bubbles (Blower et al., 2001). This ultimately produced a relatively low-vesicularity bubble suspension,

falling below the 74-85 vol.% vesicularity range typical of polydisperse spherical foams produced during Plinian eruptions (Proussevitch et al., 1993; Cashman and Mangan, 1994).

The size distribution derived from de-coalesced datasets represent bubble conditions prior to the latest stages of coalescence (Klug and Cashman, 1994), whereas earlier stages cannot be resolved by watershed segmentation if merged bubbles re-acquire a near-subspherical shape. The prevalent unimodal distribution of VVDs and VSDs therefore suggests that coalescence played a limited role during the early stages of bubble formation. As bubbles continued to grow, however, they eventually interconnected to form a complex vesicle network. Despite this interconnection, the short time available for bubble growth inhibited the development of sufficient permeability, preventing significant outgassing (**Fig. 8**). Notably, permeability pathways did not develop even near conduit margins, where shear-induced bubble stretching would be expected to enhance gas escape through the alignment and channelling of elongated vesicles. Tube pumice outgassing parameters (§3.4.2.) estimated along the primary elongation axis are comparable to those of "standard" subcircular pumice. As a result, closed-system degassing persisted, maintaining coupled magma-gas ascent that intensified the internal pressure buildup, directly contributing to the violent fragmentation observed during the RP eruption. The combination of rapid nucleation, limited time for growth, and restricted permeability created a system primed for explosive fragmentation.

5.3. Fragmentation criterion

We exclude the influence of external factors such as the input of external water or sudden decompression due to edifice collapse in promoting magma fragmentation and eruption explosivity, as no evidence for these processes exists in the RP tephrostratigraphic record (Fontijn et al., 2011, 2013; this study). For viscous magmas unaffected by external gases or liquid water inputs, several fragmentation criteria have been proposed to produce explosive eruptions. However, fragmentation of peralkaline magmas is complex to evaluate with conventional criteria (e.g., Shea et al., 2017) and has been associated with a combination of localised strain, bubble overpressure, and a critical bubble volume fraction (e.g., Polacci et al., 2004; Hughes et al., 2017; Pappalardo et al., 2018; Stabile et al., 2021). To explore the conditions that led to explosivity during the RP eruption, we discuss three key fragmentation criteria: i) the strain-rate criterion (Dingwell and Webb, 1989; Dingwell, 1996; Papale, 1999); ii) the conduit-walls shear zone criterion (Gonnermann and Manga, 2003); and iii) the bubble overpressure criterion (Zhang, 1999; Spieler et al., 2004; Mueller et al., 2008).

i) The strain rate criterion is based on the effects of rapid elongational strain, induced by magma acceleration during ascent, on the structural response of magma (Dingwell and Webb, 1989; Dingwell, 1996; Papale, 1999). In this context, fragmentation is associated with crossing the glass transition threshold which occurs when the strain rate exceeds the structural relaxation time of the magma (Dingwell and Webb, 1989; Dingwell, 1996; Papale, 1999; Gonnermann, 2015). This transition marks a shift from viscous to elastic behaviour, eventually leading to brittle failure (Gonnermann, 2015).

Fragmentation can result from either a drop in temperature below the glass transition temperature or from a sudden increase in the deformation rate (Dingwell and Webb, 1989). The strain rate criterion can be described through the Maxwell relation, where the critical strain rate (γ_{crit}) is related to the reciprocal of the relaxation time (τ) by the constant k =0.01 (Papale, 1999):

$$\gamma_{crit} = k\frac{1}{\tau} \quad (6)$$

During ascent, the elongational strain rate depends on magma acceleration and is described as dv_z/dz, or rather the dependency of magma ascent rate (v) with depth (z), where z = 0 m at the base of the conduit and increases upward. The structural relaxation time is linked to magma viscosity (μ) through the elastic modulus G = 10 GPa (Gonnermann and Manga, 2003), therefore the fragmentation criterion can be written as (Papale, 1999):

$$\frac{dv_z}{dz} > k\frac{G}{\mu} \quad (7)$$

For the RP, assuming a linear acceleration of magma from z = 0 m (P ~92 MPa) with an initial velocity v_0 = 0 m·s^{-1} to peak ascent rate of 218 m·s^{-1} (based on pumice textures recording the hypothetical maximum ascent rate at fragmentation) at z = 2296-2926 m (P ~30-13 MPa; §5.2), we can estimate a conduit-scale strain rate of 0.075-0.095 s^{-1}. Considering the relaxed viscosity (10^2-10^3 Pa·s), calculated for the RP compositions using the model of Giordano et al., (2008), at initial water concentrations (i.e., 4.82 wt.%) and temperatures (i.e., 925-975 °C), the criterion cannot be satisfied (**Fig. 11a-b**). We acknowledge that the assumption of linear acceleration is a simplification, as conduit flow models predict strongly nonlinear increases in ascent rates at shallow depths (Papale, 1999; Gonnermann and Manga, 2003, 2007; Campagnola et al., 2016; La Spina et al., 2021), driven by rapid increases in gas volume fraction and buoyancy. Nevertheless, the criterion cannot be satisfied for the given relaxation state, even if strain is assumed to localize within the shallowest few metres of ascent (corresponding to the last ~0.1 MPa of decompression).

However, upon ascent, magma rheology is expected to change markedly due to processes such as water exsolution and bubble expansion cooling (Mastin and Ghiorso, 2001; Gonnermann and Manga, 2007), potentially increasing viscosity by 2-3 orders of magnitude. Different processes significantly influence magma temperature (Mastin and Ghiorso, 2001; Gonnermann and Manga, 2007 and references therein): while friction at the conduit walls may heat the system—potentially inducing local bubble nucleation (Lavallée et al., 2015)—cooling effects like melt and gas expansion, as well as gas exsolution, dominate, especially in fast ascending magmas with large conduit radius. The system therefore can be subjected to an overall cooling trend, with gas temperature decreasing by up to 500 °C over a 50 MPa decompression (Mastin and Ghiorso, 2001). A simplified temperature balance can be derived by considering a single-phase, perfect gas system, where only the gas expansion effect is accounted for, as outlined in Eq. (21) of Mastin and Ghiorso (2001). This simplification excludes the contributions from melt expansion and gas exsolution, which together account for only 10–15% of the

total cooling. Although decompression-induced microlite crystallisation could theoretically generate a heating effect counteracting gas exsolution undercooling (Mastin and Ghiorso, 2001; Blundy et al., 2006), syn-eruptive microlite crystallisation in RP magmas was extremely limited, preventing any significant crystallisation-related heating. Using this approach, we estimated a minimum temperature drop up to ~200 °C for magma ascending from pressures of 40 MPa to 13 MPa.

We therefore tested the strain rate criterion for a temperature drop down to 725 °C and a gradient of water content spanning the concentrations recorded in melt embayments. Additionally, we also evaluated the water concentration potentially reached by the melt at the inferred quenching pressure of 13 MPa (i.e., ~0.83 wt.%), estimated by Di Matteo et al. (2004) solubility model. Nevertheless, to satisfy the criterion under the most extreme conditions—lowest water content and highest degree of cooling—a minimum strain rate of 1.74 s^{-1} must be exceeded, which would require an unlikely localisation of magma acceleration within the uppermost ~90 m beneath the fragmentation surface (**Fig. 11a-b**). This may indicate that the magma viscosity of these compositions is generally too low to induce strain rate-dependent fragmentation caused solely by ascent-induced elongation.

ii) The conduit wall shear zone criterion governs fragmentation at the melt-bedrock interface due to frictional forces created by the viscous flow of magma (Gonnermann and Manga, 2003). Shear-induced fragmentation occurs locally at the conduit walls when stress concentrates inducing a non-Newtonian response in the liquid and leading to the breakup of molecular bonds in a shear-thinning process (Dingwell, 1996; Gonnermann and Manga, 2003; Gonnermann, 2015). However, this localized process does not always generate explosive eruptions. In some cases, for highly viscous magma, it can increase permeability through melt and bedrock fractures, which facilitate outgassing and may promote effusive rather than explosive behaviour (Gonnermann and Manga, 2003).

Like the strain-rate criterion, the shear zone criterion is dependent on melt viscosity at zero frequency and shear-strain rate, which is linked to conduit geometry, as postulated by Gonnermann and Manga (2003):

$$\frac{Q}{\pi R^3} \approx C G \mu_{crit}^{-0.9} \tag{8}$$

where Q is the volumetric flow rate ($m^3 \cdot s^{-1}$) through a cylindrical conduit of radius R (m), C is a fitting parameter equal to 0.01 $(Pa \cdot s)^{-0.1}$, and G = 10 GPa is the elastic modulus at infinite frequency. The fragmentation criterion is satisfied when melt viscosity exceeds the critical viscosity (μ_{crit}).

To account for uncertainty in μ_{crit}, 5000 Monte Carlo simulations we performed, randomly sampling from the distributions of each input parameter. Q was obtained by dividing the MDR by the magma bulk density (melt+bubbles), which was derived from the melt density (2250 ± 10 $kg \cdot m^{-3}$; Cappelli et al., 2025) multiplied by the complementary value of ash average vesicularity (0.63 ± 0.05). MDR values were randomly sampled from the peak MDR range estimated by Fontijn et al. (2011) (2.8–4.8 × 10^8 $kg \cdot s^{-1}$). A statistical distribution of conduit radii was then obtained via 5000 Monte Carlo simulations

of Eq. (16) in Shea (2017), incorporating the given range of decompression rates (5.9 ± 2.4 MPa·s^{-1}), bulk densities, and MDRs.

The resulting critical viscosity is extremely high (~10^8 Pa·s) and cannot be exceeded even for minimum water contents and a temperature drop to 725 °C (**Fig. 11c**). Furthermore, fragmentation at conduit walls could have been mitigated by the cogenetic effect of viscous dissipation heating (Mastin, 2005) or by the lubricating action of compressible fusiform bubbles—as indicated by the presence of tube pumices in the deposit—which dissipated shear stress. Additionally, no evidence of shear-produced banded obsidians, indicative of prolonged cycles of fragmentation, deformation, and reannealing, (Gonnermann and Manga, 2003), was found in the deposit. While we cannot exclude that such a process occurred locally at conduit margins, it was most likely ineffective in triggering the fragmentation of the entire system.

iii) The bubble overpressure criterion predicts magma fragmentation when the gas pressure inside bubbles exceeds the tensile strength of the magma, causing bubble-wall failure (Zhang, 1999; Gonnermann and Manga, 2003; Spieler et al., 2004; Mueller et al., 2008). During magma ascent, bubbles expand due to volatile diffusion and decompression. However, if this expansion is hindered or retarded by factors such as viscous resistance, surface tension, or volumetric constraints, bubbles can develop internal overpressure in disequilibrium with the melt pressure (Zhang, 1999). In viscous magmas, bubbles rise at the same rate as the surrounding melt, limiting the overpressure dissipation through outgassing. This buildup of overpressure can lead to an energetic release once it surpasses a critical instability threshold, triggering fragmentation and propagating a shock decompression wave downward through the conduit (Gonnermann, 2015). The growth of gas overpressure depends on the efficiency of outgassing, which is related to the permeability (k_D) and vesicularity (φ) of the magma. These parameters have been experimentally linked to the critical overpressure necessary for fragmentation by the relationship (Mueller et al., 2008):

$$\Delta P_{crit} = \frac{a\sqrt{k_D} + \sigma_m}{\varphi} \quad (9)$$

where a and σ_m are fitting parameters equivalent to 8.21 ×10^5 MPa·m^{-1} and 1.54 MPa respectively.

To calculate the pre-fragmentation gas bubble overpressure for the RP eruption, we used a simplified Rayleigh-Plesset equation (Lensky et al., 2001; Gonnermann, 2015):

$$\Delta P = \frac{2\sigma}{r} + 4\mu\frac{G}{r} \quad (10)$$

which relates the bubble average radius r (m) to bubble growth rate G (m·s^{-1}), where σ is the bubble surface tension, assumed to be ~0.1 N·m^{-1} (Gonnermann, 2015). We tested the criterion across a range of viscosities (μ), iteratively adjusting water concentration and temperature until the bubble overpressure exceeded the critical threshold of 3.54 ±0.21 MPa derived from Eq. (9). The criterion is satisfied for the minimum water concentrations recorded in the embayment glasses and for temperatures

≤ 725 °C, while for water contents at quenching pressure it results satisfied for temperatures of ~760 °C (**Fig. 11d**).

Bubble growth during magma ascent is controlled by diffusion-driven volatile exsolution and decompression-induced gas expansion. Water concentration gradients in embayments indicate that diffusion was not particularly effective in promoting exsolution. This is especially relevant considering that exsolution itself increases the viscosity of the melt around bubbles, thereby inhibiting further diffusion. As a result, gas expansion likely played a dominant role. However, we propose that growth was eventually limited, potentially restricting undercooling of the entire melt system. Instead, intense localised thermal gradients potentially formed at the bubble-melt interface inducing bubble wall rupture (Mastin and Ghiorso, 2001; Hughes et al., 2017), further supporting the bubble overpressure criterion.

In summary, we find that the bubble overpressure fragmentation criterion is satisfied, driven by drastic changes in melt viscosity induced by water exsolution and melt cooling. The conditions for RP explosivity are therefore linked to pre-eruptive water concentrations. Although these concentrations are lower than those observed in other phonolitic and trachytic systems (Carroll and Blank, 1997; Berndt et al., 2001; Romano et al., 2021), their combination with rapid ascent rates and initial overheating prevented microlite crystallisation and induced delayed bubble nucleation capable of forming an extremely energetic bubble suspension. We infer that the interplay between relatively shallow storage conditions and rapid ascent velocity was critical in governing magma behaviour. RP reservoir was likely destabilised by input of a volatile-rich magma from beneath (Fontijn et al., 2013; Cappelli et al., 2025). Such high ascent rates were possibly facilitated by the reservoir's relatively low density and viscosity, which allowed the rapid rise of hot, microlite-free, and pressurised magma. Shallow magmatic conditions are not unusual for phonolitic-trachytic reservoirs associated with explosive eruptions (e.g., Andújar et al., 2008; Scaillet et al., 2008). It has been documented how explosivity in such magmas is marked by the positive correlation of pressure and water concentration of reservoirs (Andújar and Scaillet, 2012), highlighting an interdependence between shallow conditions and low water content in driving explosive activity, even under undersaturated conditions (Andújar and Scaillet, 2012). The case for the RP eruption aligns with this trend while remaining unique in its specific conditions, offering a valuable comparison for other little-studied alkaline systems along the EAR that might share similar pre-eruptive shallow conditions.

6. Conclusions

In this study, we combined 2D and 3D textural methods with embayment water diffusivity-dependent speedometers to unravel the conduit processes driving the explosivity of the Rungwe Pumice eruption. We demonstrated how, during unrest, the rapid ascent of hot magma from shallow crustal levels inhibited microlite crystallisation. The absence of nucleation sites delayed bubble formation, leading to spontaneous nucleation at high supersaturation pressures. Energetic bubble nucleation outburst further accelerated magma ascent. However, bubble growth was constrained by the packing of

bubbles into an intricate pore network and the limited time available before brittle fragmentation. This process led to bubble overpressure, which could not dissipate via outgassing through the vesicle network due to rapid ascent and insufficient time for the development of permeability pathways. Eventually, bubble overpressure overcame the critical threshold when rheological changes induced by temperature drops and water exsolution (likely concentrated at bubble interconnections) allowed the brittle failure of the melt. Our model highlights the challenges in applying conventional fragmentation criteria to microlite-free and phenocryst-poor, relatively low-viscosity peralkaline magmas. In such systems, significant rheological alterations must be inferred to explain fragmentation. These findings suggest that further experimental work is essential to better characterise the fragmentation dynamics of these magmatic systems.

Data availability statement

The raw 3DXCT scan data are available in the GFZ Data Services repository at: https://doi.org/10.5880/fidgeo.2025.023

Acknowledgements

LC was founded by an F.R.S.-FNRS Aspirant grant. Samples were collected with support from Fonds Wetenschappelijk Onderzoek Aspirant Fellowship (2006-2010) awarded to KF; in this follow-up study, KF was supported by F.R.S.-FNRS MIS Grant F.451520F and PDR Grant T.0121.24. µXCT analyses performed with funding from the European Union's Horizon Europe research and innovation program under grant agreement No 101131765 (EXCITE2) for Transnational Access conducted at Istituto Nazionale di Geofisica e Vulcanologia – Osservatorio Vesuviano (INGV-OV). The Raman equipment of KU Leuven was acquired via the medium-scale research infrastructure grant Raman-SIM2 (grant no I000718N). We gratefully thank the Editor, Jamie Farquharson, for handling the submission process, and the two anonymous reviewers, whose constructive feedback greatly improved the quality of the data presentation and discussion.

Author contributions

This study was conceptualized by LC and KF. Data were collected by LC together with LP, GB, TDG, and VNS. Fieldwork was conducted by KF and facilitated by EM with contributions from SK, EA, and GGJE. LC handled data curation and drafted the manuscript. KF reviewed the first draft. All authors contributed to scientific discussion and manuscript revision.

References

Andújar J., Costa F., Martí J., Wolff J. A., & Carroll M. R. (2008). Experimental constraints on the pre-eruptive conditions of the phonolitic magma from the caldera-forming the Abrigo eruption, Tenerife (Canary Islands). *Chemical Geology*, 257(3–4), 173–191. https://doi.org/10.1016/j.chemgeo.2008.08.012

Andújar J., & Scaillet B. (2012). Relationships between pre-eruptive conditions and eruptive styles of phonolite-trachyte magmas. *Lithos*, 152, 122–131. https://doi.org/10.1016/j.lithos.2012.05.009

Aravena A., Cioni R., de' Michieli Vitturi M., Pistolesi M., Ripepe M., & Neri A. (2018). Evolution of Conduit Geometry and Eruptive Parameters During Effusive Events. *Geophysical Research Letters*, 45(15), 7471–7480. https://doi.org/10.1029/2018GL077806

Arganda-Carreras I., Kaynig V., Rueden C., Eliceiri K. W., Schindelin J., Cardona A., & Seung H. S. (2017). Trainable Weka Segmentation: A machine learning tool for microscopy pixel classification. *Bioinformatics*, 33(15), 2424–2426. https://doi.org/10.1093/bioinformatics/btx180

Bamber E. C., La Spina G., Arzilli F., Polacci M., Mancini L., de' Michieli Vitturi M., Andronico D., Corsaro R. A., & Burton M. R. (2024). Outgassing behaviour during highly explosive basaltic eruptions. *Communications Earth and Environment*, 5(1). https://doi.org/10.1038/s43247-023-01182-w

Berndt J., Holtz F., & Koepke J. (2001). Experimental constraints on storage conditions in the chemically zoned phonolitic magma chamber of the Laacher See volcano. *Contributions to Mineralogy and Petrology*, 140, 469–486.

Blower J. D., Keating J. P., Mader H. M., & Phillips J. C. (2001). Inferring volcanic degassing processes from vesicle size distributions. *Geophysical Research Letters*, 28(2), 347–350. https://doi.org/10.1029/2000GL012188

Blower J. D., Keating J. P., Mader H. M., & Phillips J. C. (2002). The evolution of bubble size distributions in volcanic eruptions. *Journal of Volcanology and Geothermal Research*, 120, 1–23.

Blundy J., Cashman K., & Humphreys M. (2006). Magma heating by decompression-driven crystallization beneath andesite volcanoes. *Nature*, 443(7107), 76–80. https://doi.org/10.1038/nature05100

Browne B., & Szramek L. (2015). Rates of Magma Ascent and Storage. In *The Encyclopedia of Volcanoes* (pp. 203–214). Elsevier. https://doi.org/10.1016/B978-0-12-385938-9.00009-2

Browning J., Drymoni K., & Gudmundsson A. (2015). Forecasting magma-chamber rupture at Santorini volcano, Greece. *Scientific Reports*, 5. https://doi.org/10.1038/srep15785

Buono G., Caliro S., Macedonio G., Allocca V., Gamba F., & Pappalardo L. (2023). Exploring microstructure and petrophysical properties of microporous volcanic rocks through 3D multiscale and super-resolution imaging. *Scientific Reports*, 13(1). https://doi.org/10.1038/s41598-023-33687-x

Buono G., Fanara S., Macedonio G., Palladino D. M., Petrosino P., Sottili G., & Pappalardo L. (2020). Dynamics of degassing in evolved alkaline magmas: Petrological, experimental and theoretical

insights. In *Earth-Science Reviews* (Vol. 211). Elsevier B.V. https://doi.org/10.1016/j.earscirev.2020.103402

Burgisser A., Chevalier L., Gardner J. E., & Castro J. M. (2017). The percolation threshold and permeability evolution of ascending magmas. *Earth and Planetary Science Letters*, 470, 37–47. https://doi.org/10.1016/j.epsl.2017.04.023

Cáceres F., Scheu B., Colombier M., Hess K. U., Feisel Y., Ruthensteiner B., & Dingwell D. B. (2022). The roles of microlites and phenocrysts during degassing of silicic magma. *Earth and Planetary Science Letters*, 577. https://doi.org/10.1016/j.epsl.2021.117264

Campagnola S., Romano C., Mastin L. G., & Vona A. (2016). Confort 15 model of conduit dynamics: applications to Pantelleria Green Tuff and Etna 122 BC eruptions. *Contributions to Mineralogy and Petrology*, 171(6). https://doi.org/10.1007/s00410-016-1265-5

Cappelli, L., Wallace, P. A., Ernst, G. G. J., Mbede, E., Kwelwa, S., Abdallah, E., & Fontijn, K. (2025). Pre-Eruptive Reservoir Conditions of the Peralkaline Rungwe Pumice Plinian Eruption (Tanzania) from Haüyne-Hosted Melt Inclusions. *Journal of Petrology*, 66(9). https://doi.org/10.1093/petrology/egaf079

Carey S., & Sigurdsson H. (1989). The intensity of plinian eruptions. *Bulletin of Volcanology*, 51, 28–40.

Carey S., & Sparks R. S. J. (1986). Quantitative models of the fallout and dispersal of tephra from volcanic eruption columns. *Bulletin of Volcanology*, 48(2–3), 109–125. https://doi.org/10.1007/BF01046546

Carroll M. R., & Blank J. G. (1997). The solubility of H_2O in phonolitic melts. *American Mineralogist*, 82, 549–556.

Cashman K. V, & Mangan M. T. (1994). Chapter 11b. Physical Aspects of Magmatic Degassing II. Constraints on vesiculation processes from textural studies of eruptive products. In M. R. Carroll & J. R. Holloway (Eds.), *Volatiles in Magmas* (pp. 447–478). De Gruyter. https://doi.org/doi:10.1515/9781501509674-018

Cassidy M., Manga M., Cashman K., & Bachmann O. (2018). Controls on explosive-effusive volcanic eruption styles. *Nature Communications*, 9(1). https://doi.org/10.1038/s41467-018-05293-3

Cioni R. (2000). Volatile content and degassing processes in the AD 79 magma chamber at Vesuvius (Italy). *Contributions to Mineralogy and Petrology*, 140(1), 40–54. https://doi.org/10.1007/s004100000167

Cioni R., Pistolesi M., & Rosi M. (2015). Plinian and Subplinian Eruptions. In *The Encyclopedia of Volcanoes* (pp. 519–535). Elsevier. https://doi.org/10.1016/b978-0-12-385938-9.00029-8

Cooper S. J., Bertei A., Shearing P. R., Kilner J. A., & Brandon N. P. (2016). TauFactor: An open-source application for calculating tortuosity factors from tomographic data. *SoftwareX*, 5, 203–210. https://doi.org/10.1016/j.softx.2016.09.002

Costa F., Shea T., & Ubide T. (2020). Diffusion chronometry and the timescales of magmatic processes. In *Nature Reviews Earth and Environment* (Vol. 1, Issue 4, pp. 201–214). Springer Nature. https://doi.org/10.1038/s43017-020-0038-x

deGraffenried R. L., & Shea T. (2021). Using Volatile Element Concentration Profiles in Crystal-Hosted Melt Embayments to Estimate Magma Decompression Rate: Assumptions and Inherited Errors. *Geochemistry, Geophysics, Geosystems*, 22(5). https://doi.org/10.1029/2021GC009672

Degruyter W., Bachmann O., Burgisser A., & Manga M. (2012). The effects of outgassing on the transition between effusive and explosive silicic eruptions. *Earth and Planetary Science Letters*, 349–350, 161–170. https://doi.org/10.1016/j.epsl.2012.06.056

Di Genova D., Romano C., Hess K. U., Vona A., Poe B. T., Giordano D., Dingwell D. B., & Behrens H. (2013). The rheology of peralkaline rhyolites from Pantelleria Island. *Journal of Volcanology and Geothermal Research*, 249, 201–216. https://doi.org/10.1016/j.jvolgeores.2012.10.017

Di Genova D., Sicola S., Romano C., Vona A., Fanara S., & Spina L. (2017). Effect of iron and nanolites on Raman spectra of volcanic glasses: A reassessment of existing strategies to estimate the water content. *Chemical Geology*, 475, 76–86. https://doi.org/10.1016/j.chemgeo.2017.10.035

Di Matteo V., Carroll M. R., Behrens H., Vetere F., & Brooker R. A. (2004). Water solubility in trachytic melts. *Chemical Geology*, 213(1–3), 187–196. https://doi.org/10.1016/j.chemgeo.2004.08.042

Dingwell D. B. (1996). Volcanic Dilemma: Flow or Blow? *Science*, 273, 1054–1055.

Dingwell D. B., & Webb S. L. (1989). Structural Relaxation in Silicate Melts and Non-Newtonian Melt Rheology in Geologic Processes. *Physics and Chemistry of Minerals*, 16, 508–516.

Dragonfly 3D World (2024) for Windows; Comet Technologies Canada Inc., Montreal, Canada; software available at: https://www.theobjects.com/dragonfly

Ebinger C. J., Deino A. L., Drake E., & Tesha A. L. (1989). Chronology of volcanism and rift basin propagation: Rungwe Volcanic Province, East Africa. *Journal of Geophysical Research*, 94, 15785–15803.

Ebinger C. J., Deino A. L., Tesha A. L., Becker T., & Ring U. (1993). Tectonic controls on rift basin morphology: evolution of the northern Malawi (Nyasa) Rift. *Journal of Geophysical Research*, 98(B10). https://doi.org/10.1029/93jb01392

Ebinger C. J., Keir D., Bastow I. D., Whaler K., Hammond J. O. S., Ayele A., Miller M. S., Tiberi C., & Hautot S. (2017). Crustal Structure of Active Deformation Zones in Africa: Implications for Global Crustal Processes. In *Tectonics* (Vol. 36, Issue 12, pp. 3298–3332). Blackwell Publishing Ltd. https://doi.org/10.1002/2017TC004526

Edmonds M., & Woods A. W. (2018). Exsolved volatiles in magma reservoirs. *Journal of Volcanology and Geothermal Research*, 368, 13–30. https://doi.org/10.1016/j.jvolgeores.2018.10.018

Epstein N. (1989). On tortuosity and tortuosity factor. *Chemical EngineeringScience*, 44(3), 777–779.

Fanara S., Behrens H., & Zhang Y. (2013). Water diffusion in potassium-rich phonolitic and trachytic melts. *Chemical Geology*, 346, 149–161. https://doi.org/10.1016/j.chemgeo.2012.09.030

Fontijn K., Delvaux D., Ernst G. G. J., Kervyn M., Mbede E., & Jacobs P. (2010a). Tectonic control over active volcanism at a range of scales: Case of the Rungwe Volcanic Province, SW Tanzania; and hazard implications. *Journal of African Earth Sciences*, 58(5), 764–777. https://doi.org/10.1016/j.jafrearsci.2009.11.011

Fontijn K., Elburg M. A., Nikogosian I. K., van Bergen M. J., & Ernst G. G. J. (2013). Petrology and geochemistry of Late Holocene felsic magmas from Rungwe volcano (Tanzania), with implications for trachytic Rungwe Pumice eruption dynamics. *Lithos*, 177, 34–53. https://doi.org/10.1016/j.lithos.2013.05.012

Fontijn K., Ernst G. G. J., Bonadonna C., Elburg M. A., Mbede E., & Jacobs P. (2011). The ~4-ka Rungwe Pumice (South-Western Tanzania): A wind-still Plinian eruption. *Bulletin of Volcanology*, 73(9), 1353–1368. https://doi.org/10.1007/s00445-011-0486-8

Fontijn K., Ernst G. G. J., Elburg M. A., Williamson D., Abdallah E., Kwelwa S., Mbede E., & Jacobs P. (2010b). Holocene explosive eruptions in the Rungwe Volcanic Province, Tanzania. *Journal of Volcanology and Geothermal Research*, 196(1–2), 91–110. https://doi.org/10.1016/j.jvolgeores.2010.07.021

Fontijn K., Williamson D., Mbede E., & Ernst G. G. J. (2012). The Rungwe Volcanic Province, Tanzania - A volcanological review. *Journal of African Earth Sciences*, 63, 12–31. https://doi.org/10.1016/j.jafrearsci.2011.11.005

Garcin Y., Williamson D., Taieb M., Vincens A., Mathé P. E., & Majule A. (2006). Centennial to millennial changes in maar-lake deposition during the last 45,000 years in tropical Southern Africa (Lake Masoko, Tanzania). *Palaeogeography, Palaeoclimatology, Palaeoecology*, 239(3–4), 334–354. https://doi.org/10.1016/j.palaeo.2006.02.002

Georgeais G., Koga K. T., Moussallam Y., & Rose-Koga E. F. (2021). Magma Decompression Rate Calculations With EMBER: A User-Friendly Software to Model Diffusion of H_2O, CO_2, and S in

Melt Embayments. *Geochemistry, Geophysics, Geosystems*, 22(7). https://doi.org/10.1029/2020GC009542

Geshi N., Yamasaki T., Miyagi I., & Conway C. E. (2021). Magma chamber decompression during explosive caldera-forming eruption of Aira caldera. *Communications Earth and Environment*, 2(1). https://doi.org/10.1038/s43247-021-00272-x

Ghiorso M. S., & Gualda G. A. R. (2015). An H_2O–CO_2 mixed fluid saturation model compatible with rhyolite-MELTS. *Contributions to Mineralogy and Petrology*, 169(6). https://doi.org/10.1007/s00410-015-1141-8

Giachetti T., Burgisser A., Arbaret L., Druitt T. H., & Kelfoun K. (2011). Quantitative textural analysis of Vulcanian pyroclasts (Montserrat) using multi-scale X-ray computed microtomography: Comparison with results from 2D image analysis. *Bulletin of Volcanology*, 73(9), 1295–1309. https://doi.org/10.1007/s00445-011-0472-1

Giordano D., & Dingwell D. B. (2003). Viscosity of hydrous Etna basalt: Implications for Plinian-style basaltic eruptions. *Bulletin of Volcanology*, 65(1), 8–14. https://doi.org/10.1007/s00445-002-0233-2

Giordano D., Russell J. K., & Dingwell D. B. (2008). Viscosity of magmatic liquids: A model. *Earth and Planetary Science Letters*, 271(1–4), 123–134. https://doi.org/10.1016/j.epsl.2008.03.038

Gonnermann H. M. (2015). Magma fragmentation. *Annual Review of Earth and Planetary Sciences*, 43, 431–458. https://doi.org/10.1146/annurev-earth-060614-105206

Gonnermann H. M., & Manga M. (2003). Explosive volcanism may not be an inevitable consequence of magma fragmentation. *Nature*, 426(6965), 432–435. https://doi.org/10.1038/nature02138

Gonnermann H. M., & Manga M. (2007). The fluid mechanics inside a volcano. In *Annual Review of Fluid Mechanics* (Vol. 39, pp. 321–356). https://doi.org/10.1146/annurev.fluid.39.050905.110207

Gurioli L., Andronico D., Bachelery P., Balcone-Boissard H., Battaglia J., Boudon G., Burgisser A., Burton M. R., Cashman K., Cichy S., Cioni R., Di Muro A., Dominguez L., D'Oriano C., Druitt T., Harris A. J. L., Hort M., Kelfoun K., Komorowski J. C., … Thordarson T. (2015). MeMoVolc consensual document: a review of cross-disciplinary approaches to characterizing small explosive magmatic eruptions. *Bulletin of Volcanology*, 77(6). https://doi.org/10.1007/s00445-015-0935-x

Harkin D. A. (1960). *The Rungwe Volcanics at the Northern End of Lake Nyasa* (1st ed.). Government Printer.

Hirth J. P., Pound G. M., & St Pierre G. R. (1970). Bubble Nucleation. *Metallurgical Transactions*, I, 938–945.

Harris M., Hosseini B., Myers M., & Bouley L. (2024). Reconciling petrologic magma ascent speedometers for the June 12th, 1991 eruption of Mount Pinatubo, Philippines. *Volcanica*, 7(1), 117–133. https://doi.org/10.30909/vol.07.01.117133

Hosseini B., Myers M. L., Watkins J. M., & Harris M. A. (2023). Are We Recording? Putting Embayment Speedometry to the Test Using High Pressure-Temperature Decompression Experiments. *Geochemistry, Geophysics, Geosystems*, 24(6). https://doi.org/10.1029/2022gc010770

Hosseini B. & Myers M. (2024). Melt embayments record multi-stage magma decompression histories. *Journal of Volcanology and Geothermal Research*, 456. https://doi.org/10.1016/j.jvolgeores.2024.108211

Houghton B. F., & Gonnermann H. M. (2008). Basaltic explosive volcanism: Constraints from deposits and models. *Chemie Der Erde*, 68(2), 117–140. https://doi.org/10.1016/j.chemer.2008.04.002

Houghton B. F., Wilson C. J. N., Del Carlo P., Coltelli M., Sable J. E., & Carey R. (2004). The influence of conduit processes on changes in style of basaltic Plinian eruptions: Tarawera 1886 and Etna 122 BC. *Journal of Volcanology and Geothermal Research*, 137(1-3), 1–14. https://doi.org/10.1016/j.jvolgeores.2004.05.009

Hughes E. C., Neave D. A., Dobson K. J., Withers P. J., & Edmonds M. (2017). How to fragment peralkaline rhyolites: Observations on pumice using combined multi-scale 2D and 3D imaging. *Journal of Volcanology and Geothermal Research*, 336, 179–191. https://doi.org/10.1016/j.jvolgeores.2017.02.020

Humphreys M. C. S., Menand T., Blundy J. D., & Klimm K. (2008). Magma ascent rates in explosive eruptions: Constraints from H_2O diffusion in melt inclusions. *Earth and Planetary Science Letters*, 270(1–2), 25–40. https://doi.org/10.1016/j.epsl.2008.02.041

Hutchison W., Mather T. A., Pyle D. M., Boyce A. J., Gleeson M. L. M., Yirgu G., Blundy J. D., Ferguson D. J., Vye-Brown C., Millar I. L., Sims K. W. W., & Finch A. A. (2018). The evolution of magma during continental rifting: New constraints from the isotopic and trace element signatures of silicic magmas from Ethiopian volcanoes. *Earth and Planetary Science Letters*, 489, 203–218. https://doi.org/10.1016/j.epsl.2018.02.027

Iacovino K., Matthews S., Wieser P. E., Moore G. M., & Bégué F. (2021). VESIcal Part I: An Open-Source Thermodynamic Model Engine for Mixed Volatile (H_2O-CO_2) Solubility in Silicate Melts. *Earth and Space Science*, 8(11). https://doi.org/10.1029/2020EA001584

Jochum K. P., Stoll B., Herwig K., Willbold M., Hofmiann A. W., Amini M., Aarburg S., Abouchami W., Hellebrand E., Mocek B., Raczek I., Stracke A., Alard O., Bouman C., Becker S., Dücking M., Brätz H., Klemd R., De Bruin D., … Woodhead J. D. (2006). MPI-DING reference glasses for in

situ microanalysis: New reference values for element concentrations and isotope ratios. *Geochemistry, Geophysics, Geosystems*, 7(2). https://doi.org/10.1029/2005GC001060

Kaminski E., & Jaupart C. (1997). Expansion and quenching of vesicular magma fragments in Plinian eruptions. *Journal of Geophysical Research: Solid Earth*, 102(6), 12187–12203. https://doi.org/10.1029/97jb00622

Klug C., Cashman K., & Bacon C. (2002). Structure and physical characteristics of pumice from the climactic eruption of Mount Mazama (Crater Lake), Oregon. *Bulletin of Volcanology*, 64(7), 486–501. https://doi.org/10.1007/s00445-002-0230-5

Klug C., & Cashman K. V. (1994). Vesiculation of May 18, 1980, Mount St. Helens magma. *Geology*, 22, 468–472.

La Spina G., Arzilli F., Llewellin E. W., Burton M. R., Clarke A. B., de' Michieli Vitturi M., Polacci M., Hartley M. E., Di Genova D., & Mader H. M. (2021). Explosivity of basaltic lava fountains is controlled by magma rheology, ascent rate and outgassing. *Earth and Planetary Science Letters*, 553. https://doi.org/10.1016/j.epsl.2020.116658

La Spina G., de' Michieli Vitturi M., & Clarke A. B. (2017). Transient numerical model of magma ascent dynamics: application to the explosive eruptions at the Soufrière Hills Volcano. *Journal of Volcanology and Geothermal Research*, 336, 118–139. https://doi.org/10.1016/j.jvolgeores.2017.02.013

Lavallée Y., Dingwell D. B., Johnson J. B., Cimarelli C., Hornby A. J., Kendrick J. E., Von Aulock F. W., Kennedy B. M., Andrews B. J., Wadsworth F. B., Rhodes E., & Chigna G. (2015). Thermal vesiculation during volcanic eruptions. *Nature*, 528(7583), 544–547. https://doi.org/10.1038/nature16153

Legland D., Arganda-Carreras I., & Andrey P. (2016). MorphoLibJ: Integrated library and plugins for mathematical morphology with ImageJ. *Bioinformatics*, 32(22), 3532–3534. https://doi.org/10.1093/bioinformatics/btw413

Lensky N. G., Lyakhovsky V., & Navon O. (2001). Radial variations of melt viscosity around growing bubbles and gas overpressure in vesiculating magmas. *Earth and Planetary Science Letters*, 186, 1–6.

Liedl A., Buono G., Lanzafame G., Dabagov S. B., Della Ventura G., Hampai D., Mancini L., Marcelli A., & Pappalardo L. (2019). A 3D imaging textural characterization of pyroclastic products from the 1538 AD Monte Nuovo eruption (Campi Flegrei, Italy). *Lithos*, 340–341, 316–331. https://doi.org/10.1016/j.lithos.2019.05.010

Liu Y., Anderson A. T., & Wilson C. J. N. (2007). Melt pockets in phenocrysts and decompression rates of silicic magmas before fragmentation. *Journal of Geophysical Research: Solid Earth*, 112(6). https://doi.org/10.1029/2006JB004500

Macdonald R., & Scaillet B. (2006). The central Kenya peralkaline province: Insights into the evolution of peralkaline salic magmas. *Lithos*, 91(1–4), 59–73. https://doi.org/10.1016/j.lithos.2006.03.009

Macedonio G., Dobran F., & Neri A. (1994). Erosion processes in volcanic conduits and application to the AD 79 eruption of Vesuvius. *Earth and Planetary Science Letters*, 121, 137–152. https://doi.org/10.1016/0012-821X(94)90037-X.

Marti J., Soriano C., & Dingwell D. B. (1999). Tube pumices as strain markers of the ductile-brittle transition in magma fragmentation. *Nature*, 402, 650–653.

Mastin L. G. (2005). The controlling effect of viscous dissipation on magma flow in silicic conduits. *Journal of Volcanology and Geothermal Research*, 143(1–3), 17–28. https://doi.org/10.1016/j.jvolgeores.2004.09.008

Mastin L. G., & Ghiorso M. S. (2001). Adiabatic temperature changes of magma-gas mixtures during ascent and eruption. *Contributions to Mineralogy and Petrology*, 141(3), 307–321. https://doi.org/10.1007/s004100000210

Mourtada-Bonnefoi C. C., & Laporte D. (2004). Kinetics of bubble nucleation in a rhyolitic melt: An experimental study of the effect of ascent rate. *Earth and Planetary Science Letters*, 218(3–4), 521–537. https://doi.org/10.1016/S0012-821X(03)00684-8

Mueller S., Scheu B., Spieler O., & Dingwell D. B. (2008). Permeability control on magma fragmentation. *Geology*, 36(5), 399–402. https://doi.org/10.1130/G24605A.1

Newhall C. G., & Self S. (1982). The volcanic explosivity index (VEI): an estimate of the explosive magnitude for historical eruptions. *Journal of Geophysical Research*, 87(C2), 1231–1238.

Ni H., & Zhang L. (2018). A general model of water diffusivity in calc-alkaline silicate melts and glasses. *Chemical Geology*, 478, 60–68. https://doi.org/10.1016/j.chemgeo.2017.10.010

Papale P. (1999). Strain-induced magma fragmentation in explosive eruptions. *Nature*, 397, 425–428.

Pappalardo L., Buono G., Fanara S., & Petrosino P. (2018). Combining textural and geochemical investigations to explore the dynamics of magma ascent during Plinian eruptions: a Somma–Vesuvius volcano (Italy) case study. *Contributions to Mineralogy and Petrology*, 173(7). https://doi.org/10.1007/s00410-018-1486-x

Pappalardo L., Buono G., Fanara S., Yi J., Shan X., Guo Z., Zhang M., & Ventura G. (2023). The role of CO_2 flushing in triggering the 'Millennium' eruption and recent unrests at Changbaishan volcano

(China/North Korea). *International Geology Review*, 65(5), 706–719. https://doi.org/10.1080/00206814.2022.2065544

Pappalardo L., & Mastrolorenzo G. (2012). Rapid differentiation in a sill-like magma reservoir: A case study from the Campi Flegrei caldera. *Scientific Reports*, 2. https://doi.org/10.1038/srep00712

Polacci M., Mancini L., & Baker D. R. (2010). The contribution of synchrotron X-ray computed microtomography to understanding volcanic processes. *Journal of Synchrotron Radiation*, 17(2), 215–221. https://doi.org/10.1107/S0909049509048225

Polacci M., Papale P., Del Seppia D., Giordano D., & Romano C. (2004). Dynamics of magma ascent and fragmentation in trachytic versus rhyolitic eruptions. *Journal of Volcanology and Geothermal Research*, 131(1–2), 93–108. https://doi.org/10.1016/S0377-0273(03)00319-6

Proussevitch A. A., & Sahagian D. L. (1998). Dynamics and energetics of bubble growth in magmas: Analytical formulation and numerical modeling. *Journal of Geophysical Research: Solid Earth*, 103(8), 18223–18251. https://doi.org/10.1029/98jb00906

Proussevitch A. A., Sahagian D. L., & Kutolin V. A. (1993). Stability of foams in silicate melts. *Journal of Volcanology and Geothermal Research* (Vol. 59).

Proussevitch A. A., Sahagian D. L., & Tsentalovich E. P. (2007). Statistical analysis of bubble and crystal size distributions: Formulations and procedures. *Journal of Volcanology and Geothermal Research*, 164(3), 95–111. https://doi.org/10.1016/j.jvolgeores.2007.04.007

Romano P., Di Carlo I., Andújar J., & Rotolo S. G. (2021). Water solubility in trachytic and pantelleritic melts: An experimental study. *Comptes Rendus - Geoscience* (353). https://doi.org/10.5802/CRGEOS.75

Ronneberger O., Fischer P., & Brox T. (2015). U-net: Convolutional networks for biomedical image segmentation. In *Lecture Notes in Computer Science (including subseries Lecture Notes in Artificial Intelligence and Lecture Notes in Bioinformatics)* (Vol. 9351, pp. 234–241). Springer Verlag. https://doi.org/10.1007/978-3-319-24574-4_28

Rust A. C., & Cashman K. V. (2004). Permeability of vesicular silicic magma: Inertial and hysteresis effects. *Earth and Planetary Science Letters*, 228(1–2), 93–107. https://doi.org/10.1016/j.epsl.2004.09.025

Rust A. C., & Cashman K. V. (2011). Permeability controls on expansion and size distributions of pyroclasts. *Journal of Geophysical Research: Solid Earth*, 116(11). https://doi.org/10.1029/2011JB008494

Saria E., Calais E., Stamps D. S., Delvaux D., & Hartnady C. J. H. (2014). Present-day kinematics of the East African Rift. *Journal of Geophysical Research: Solid Earth*, 119(4), 3584–3600. https://doi.org/10.1002/2013JB010901

Scaillet B., Pichavant M., & Cioni R. (2008). Upward migration of Vesuvius magma chamber over the past 20,000 years. *Nature*, 455(7210), 216–219. https://doi.org/10.1038/nature07232

Schindelin J., Arganda-Carreras I., Frise E., Kaynig V., Longair M., Pietzsch T., Preibisch S., Rueden C., Saalfeld S., Schmid B., Tinevez J.-Y., White D. J., Hartenstein V., Eliceiri K., Tomancak P., & Cardona A. (2012). Fiji: an open-source platform for biological-image analysis. *Nature Methods*, 9(7), 676–682. https://doi.org/10.1038/nmeth.2019

Schmidt B. C., Blum-Oeste N., & Flagmeier J. (2013). Water diffusion in phonolite melts. *Geochimica et Cosmochimica Acta*, 107, 220–230. https://doi.org/10.1016/j.gca.2012.12.044

Shea T. (2017). Bubble nucleation in magmas: A dominantly heterogeneous process? *Journal of Volcanology and Geothermal Research*, 343, 155–170. https://doi.org/10.1016/j.jvolgeores.2017.06.025

Shea T., Houghton B. F., Gurioli L., Cashman K. V., Hammer J. E., & Hobden B. J. (2010). Textural studies of vesicles in volcanic rocks: An integrated methodology. *Journal of Volcanology and Geothermal Research*, 190(3–4), 271–289. https://doi.org/10.1016/j.jvolgeores.2009.12.003

Shea T., Leonhardi T., Giachetti T., Lindoo A., Larsen J., Sinton J., & Parsons E. (2017). Dynamics of an unusual cone-building trachyte eruption at Pu‘u Wa‘awa‘a, Hualālai volcano, Hawai‘i. *Bulletin of Volcanology*, 79(4). https://doi.org/10.1007/s00445-017-1106-z

Sparks R. S. J. (1978). The dynamics of bubble formation and growth in magmas: a review and analysis. *Journal of Volcanology and Geothermal Research*, 3(1), 1–37.

Spieler O., Kennedy B., Kueppers U., Dingwell D. B., Scheu B., & Taddeucci J. (2004). The fragmentation threshold of pyroclastic rocks. *Earth and Planetary Science Letters*, 226(1–2), 139–148. https://doi.org/10.1016/j.epsl.2004.07.016

Stabile P., Arzilli F., & Carroll M. R. (2021). Crystallization of peralkaline rhyolitic magmas: Pre- And syn-eruptive conditions of the Pantelleria system. *Comptes Rendus – Geoscience*, 353(S2). https://doi.org/10.5802/CRGEOS.72

Tadesse A. Z., Fontijn K., Wallace P. A., Gurioli L., Laha P., Terryn H., & Ayalew D. (2024). Eruption style and dynamics of the ~ 87 ka Baricha peralkaline rhyolite eruption in Ethiopia. *Bulletin of Volcanology*, 86(12). https://doi.org/10.1007/s00445-024-01787-9

Thomas N., Jaupart C., & Vergniolle S. (1994). On the vesicularity of pumice. *Journal of Geophysical Research*, 99(B8). https://doi.org/10.1029/94jb00650

Toramaru A. (2006). BND (bubble number density) decompression rate meter for explosive volcanic eruptions. *Journal of Volcanology and Geothermal Research*, 154(3–4), 303–316. https://doi.org/10.1016/j.jvolgeores.2006.03.027

Toramaru A. (2025). The theoretical basis for textural indices of eruption dynamics: review and new conceptual models. *Earth, Planets and Space*, 77(1). https://doi.org/10.1186/s40623-025-02146-4

Toramaru A., Noguchi S., Oyoshihara S., & Tsune A. (2008). MND (microlite number density) water exsolution rate meter. *Journal of Volcanology and Geothermal Research*, 175(1–2), 156–167. https://doi.org/10.1016/j.jvolgeores.2008.03.035

Torres-Orozco R., Capra L., Márquez-Ramírez V. H., Sosa-Ceballos G., De Plaen R. S. M., Cid H. E., Sulpizio R., & Arámbula-Mendoza R. (2024). Andesite magma genesis, conduit dynamics and variable decompression from shallow reservoirs drive contrasting PDC events at Volcán de Colima, Mexico. *Journal of Volcanology and Geothermal Research*, 453. https://doi.org/10.1016/j.jvolgeores.2024.108143

Torres-Orozco R., Cronin S. J., Pardo N., Kósik S., Ukstins I., Heinrich M., & Lee P. D. (2023). Complex decompression and fragmentation of mingled andesite magmas driving multi-phase Plinian eruptions at Mt. Taranaki, New Zealand. *Journal of Volcanology and Geothermal Research*, 433. https://doi.org/10.1016/j.jvolgeores.2022.107728

Valdivia P., Marshall A. A., Brand B. D., Manga M., & Huber C. (2022). Mafic explosive volcanism at Llaima Volcano: 3D x-ray microtomography reconstruction of pyroclasts to constrain shallow conduit processes. *Bulletin of Volcanology*, 84(1). https://doi.org/10.1007/s00445-021-01514-8

Van Gerve T. D., & Namur O. (2023). SilicH2O: a graphical user interface for processing silicate glass Raman spectra and quantifying H2O. *Volcanica*, 6(2), 405–413. https://doi.org/10.30909/vol.06.02.405413

Wallace P. A., Otieno V., Godec P., Njoroge R. W., Tubula M. S., Cappelli L., Kamau P. M., Nomade S., Mariita N. O., & Fontijn K. (2025). Temporal and spatial evolution of explosive silicic peralkaline eruptions at the Olkaria Volcanic Complex and Longonot volcano in the Southern Kenya Rift. *Journal of Volcanology and Geothermal Research*, 108275. https://doi.org/10.1016/j.jvolgeores.2025.108275

Wei W., Cai J., Xiao J., Meng Q., Xiao B., & Han Q. (2018). Kozeny-Carman constant of porous media: Insights from fractal-capillary imbibition theory. *Fuel*, 234, 1373–1379. https://doi.org/10.1016/j.fuel.2018.08.012

Wilson L., Sparks R. S. J., & Walker G. P. L. (1980). Explosive volcanic eruptions — IV. The control of magma properties and conduit geometry on eruption column behaviour. *Geophysical Journal of*

the Royal Astronomical Society, 63(1), 117–148. https://doi.org/10.1111/j.1365-246X.1980.tb02613.x

Woods A.W. (1998). Observations and models of volcanic eruption columns. In: Gilbert JS, Sparks RSJ (eds) *The physics of explosive volcanic eruptions*. *Geological Society Special Publication* 145:91–114

Zhang Y. (1999). A criterion for the fragmentation of bubbly magma based on brittle failure theory. *Nature*, 402, 648–650.

Zhou J. Q., Chen Y. F., Wang L., & Cardenas M. B. (2019). Universal Relationship Between Viscous and Inertial Permeability of Geologic Porous Media. *Geophysical Research Letters*, 46(3), 1441–1448. https://doi.org/10.1029/2018GL081413

Figures

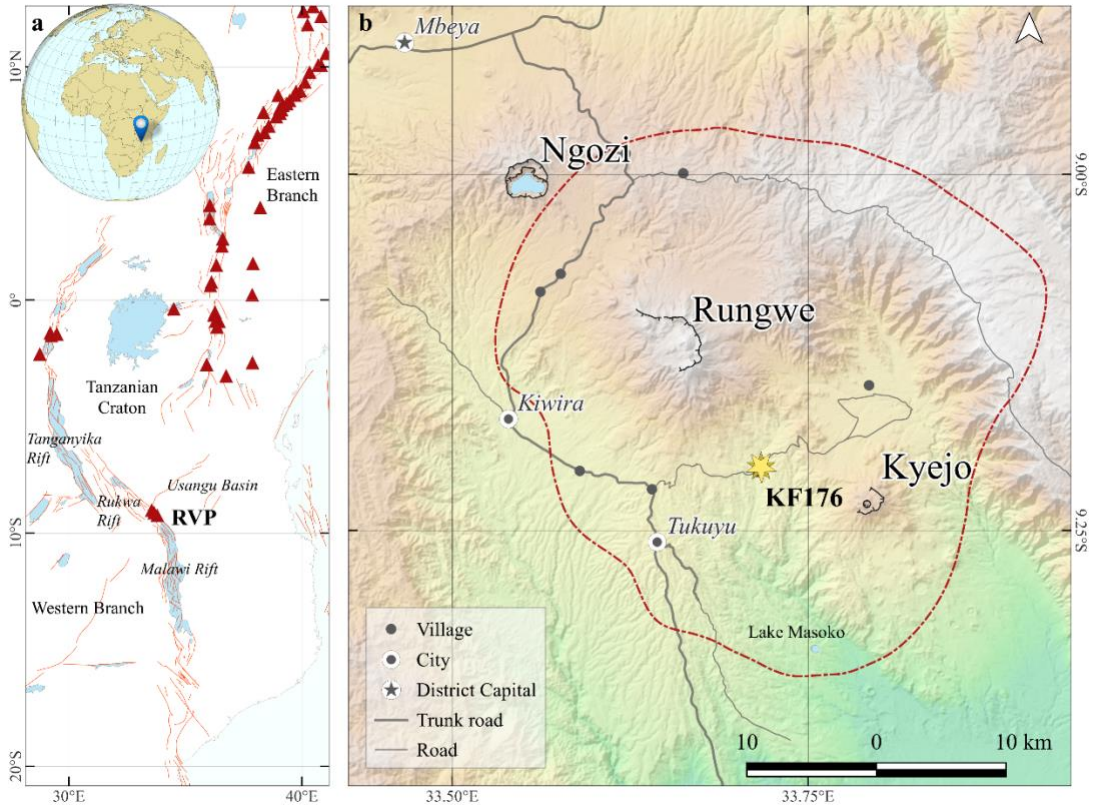

Figure 1: a) Overview of the East African Rift, showing the location of the Rungwe Volcanic Province (RVP) along the Western Branch. Major rift faults (*red lines*) and volcanic centres (*red triangles*) are indicated.; b) Close-up of the main volcanic centres within the RVP, highlighting the location of the type section KF176 (*yellow star*). The red dashed contour represents the 25 cm isopach of the Rungwe Pumice deposit (modified from Fontijn et al., 2011**).**

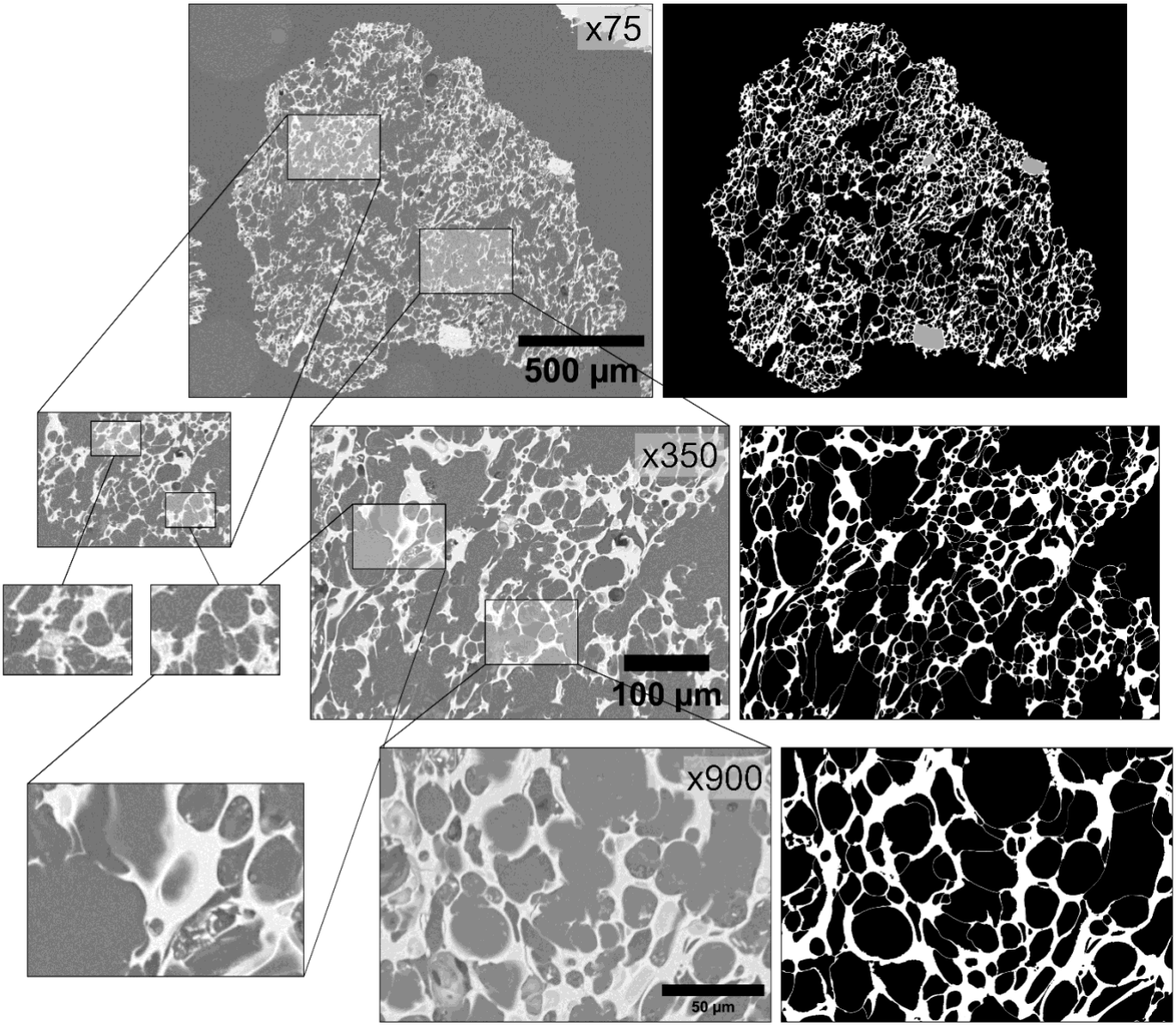

Figure 2: Image nesting method adopted for stereological conversion in FOAM, following the approach suggested by Shea (2010**) over a standard RP pumiceous clast from the middle stratigraphic horizon. For each clast, two images were selected at x350 magnification, with four additional images collected at x900 magnification within these regions. Grey-scale SEM images are shown alongside their binarized, decoalesced counterparts, where white represents pumice glass and black denotes vesicles (voids). In the x75 magnified inset, also the exterior background appears black (removed during FOAM processing), and phenocrysts are displayed in grey.**

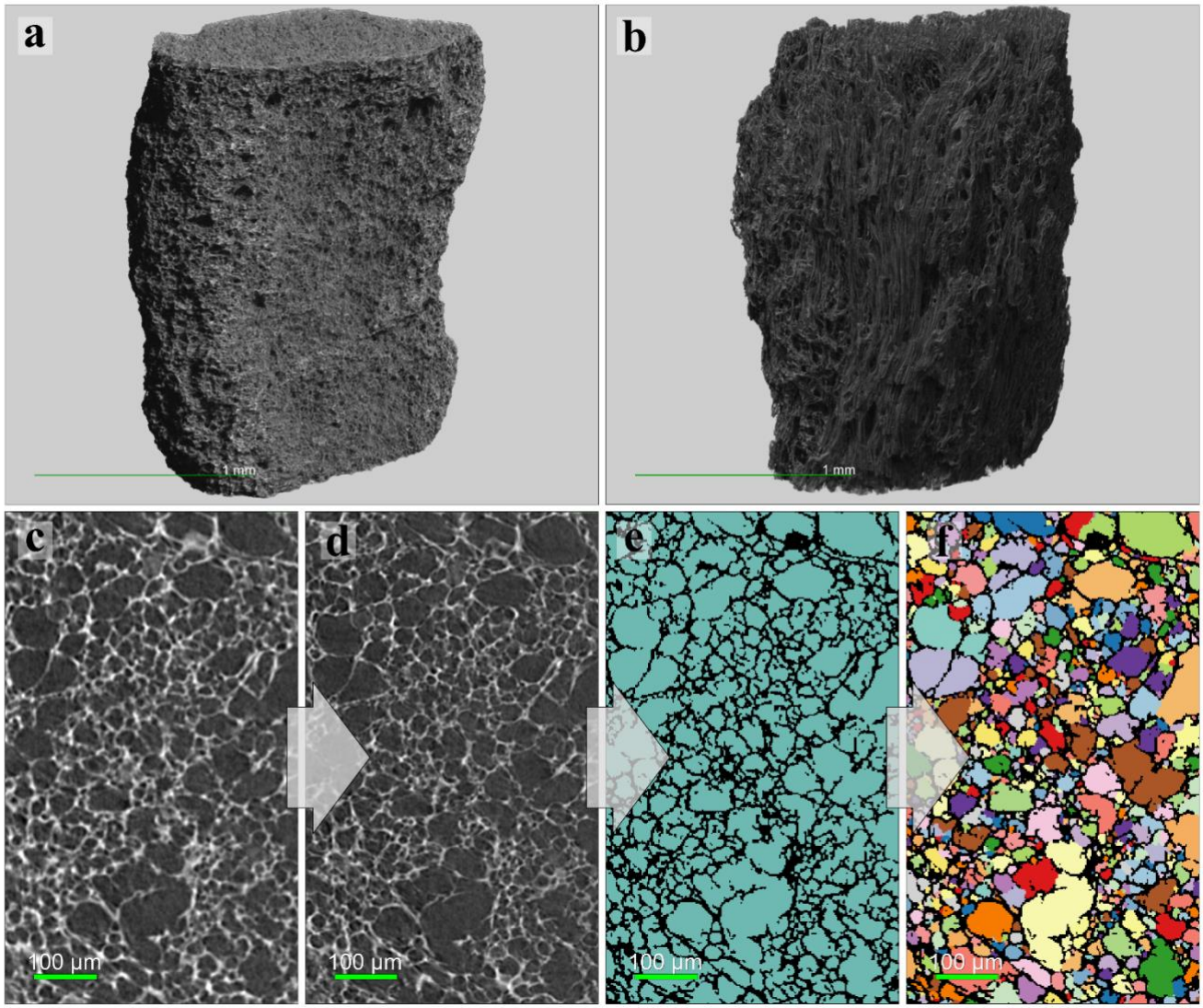

Figure 3: a) and b) µXCT volume reconstructions of a "standard" pumice from the middle horizon and the tube pumice, respectively, created in Dragonfly; c) 2D slice of a sample volume, where glass appears as light grey and vesicles as dark grey, processed through the following steps: d) application of the U-Net2D super-resolution model, e) segmentation using the U-Net2.5D segmentation model (vesicles shown in cyan and glass in black), and f) vesicle separation using the watershed algorithm.

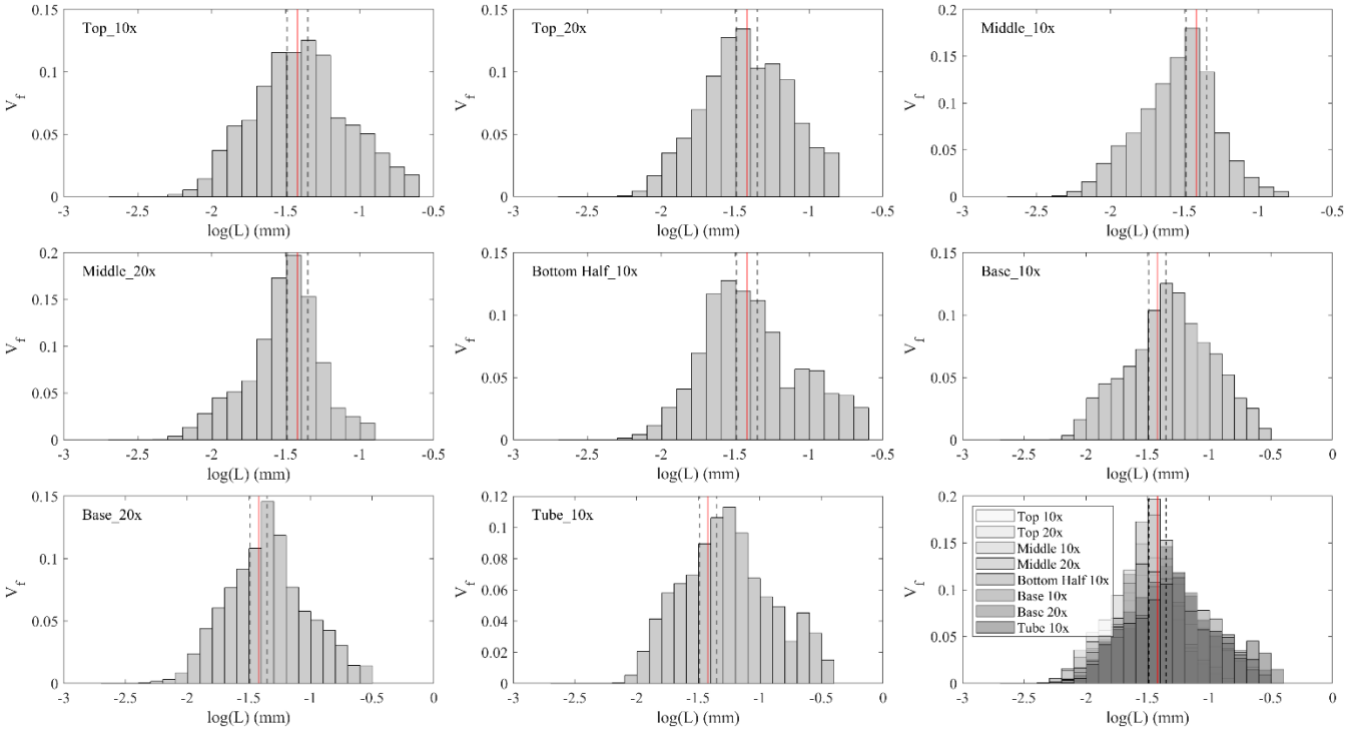

Figure 4: VVD plots for each µXCT dataset, presented individually and collectively for comparison. Most datasets exhibit lognormal, unimodal, distributions except for bottom half horizon and the tube pumice, which display a mild bimodality characterized by a secondary mode in the larger size range. This secondary mode may indicate the influence of coalescence effects on size distributions (see text for further details). The average of principal modes (red lines) corresponds to an equivalent diameter of 39 µm, with standard deviation indicated by grey dashed lines.

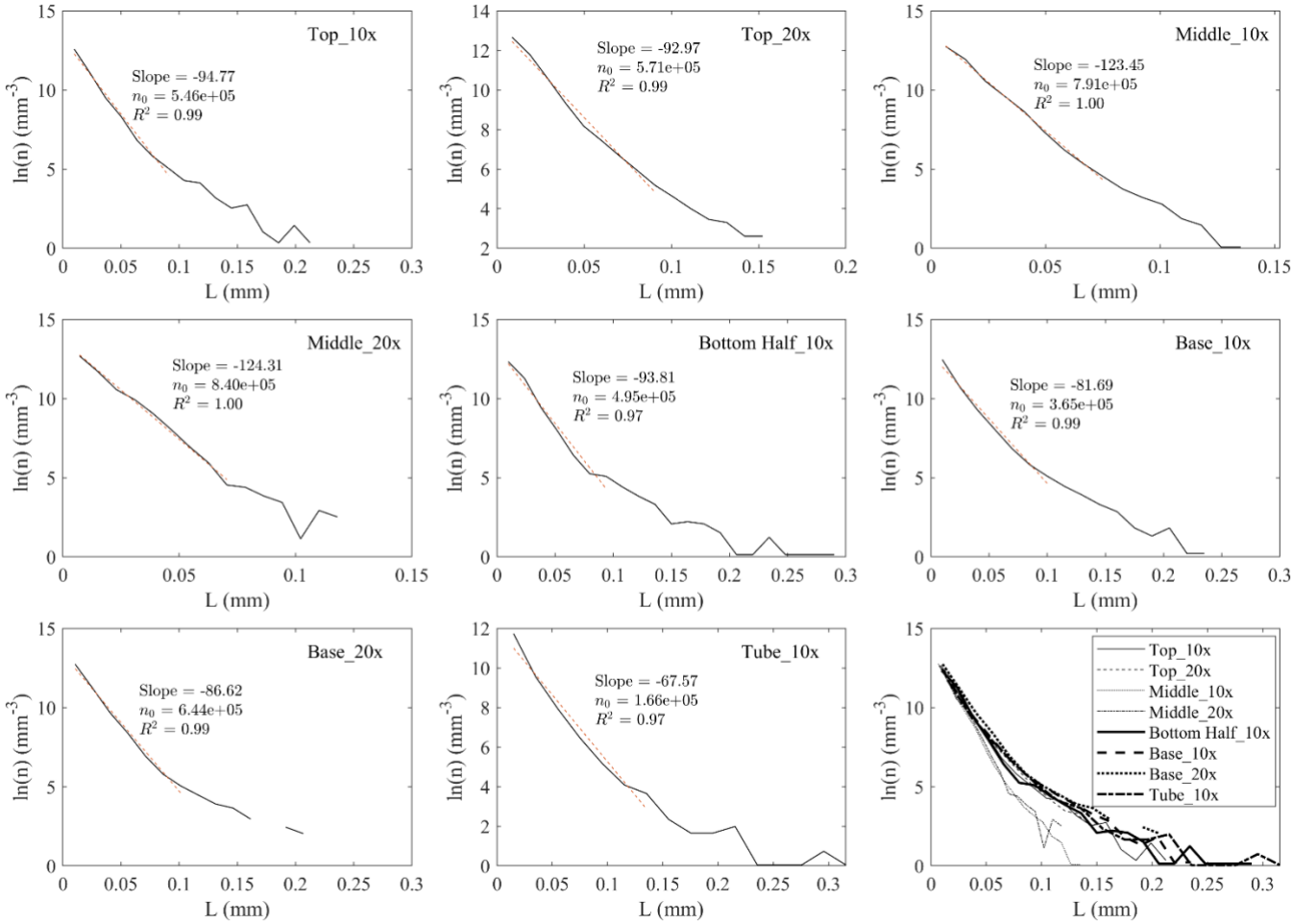

Figure 5: VSD plots for each µXCT dataset, presented individually and collectively for comparison. The slope, intercept at n_0, and goodness of fit (dashed red lines) for the linear interpolation within the smallest size range are provided for each sample.

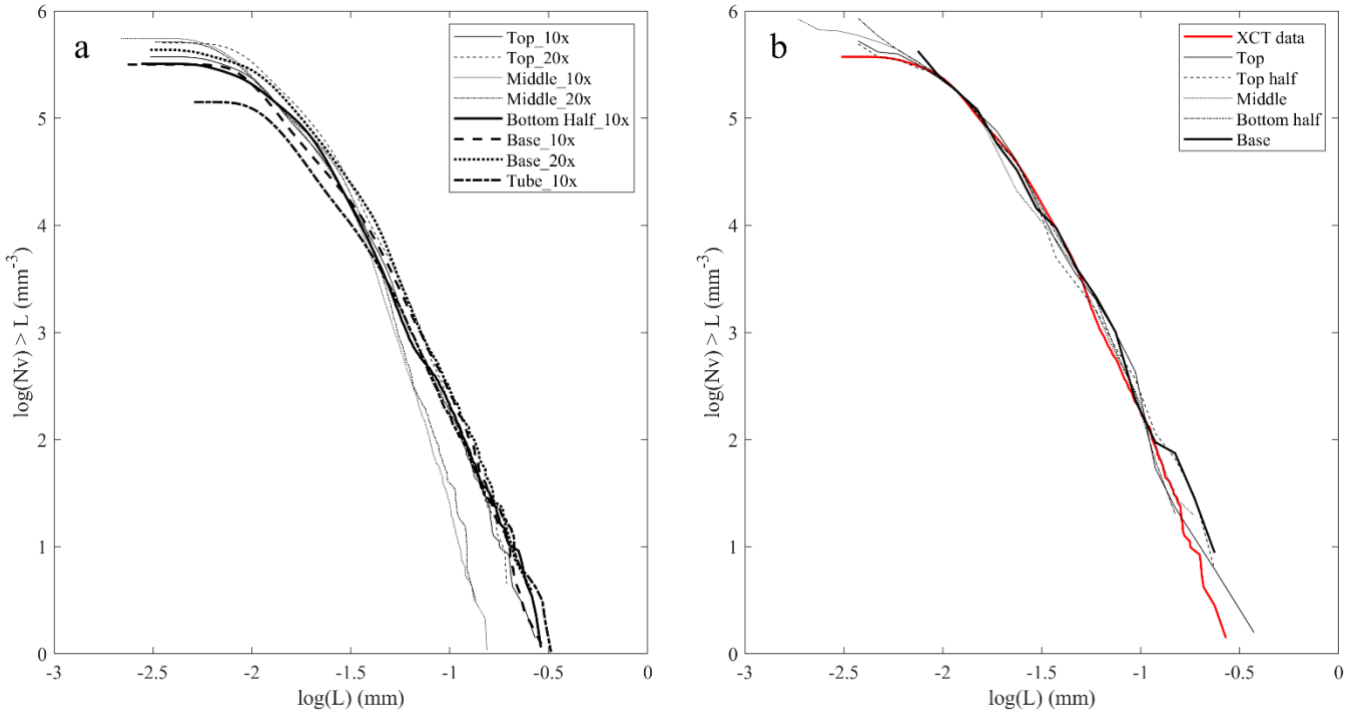

Figure 6: CVSD plots for a) µXCT datasets and b) 2D images stereologically converted with FOAM, where the µXCT trend of the base horizon is included for comparison.

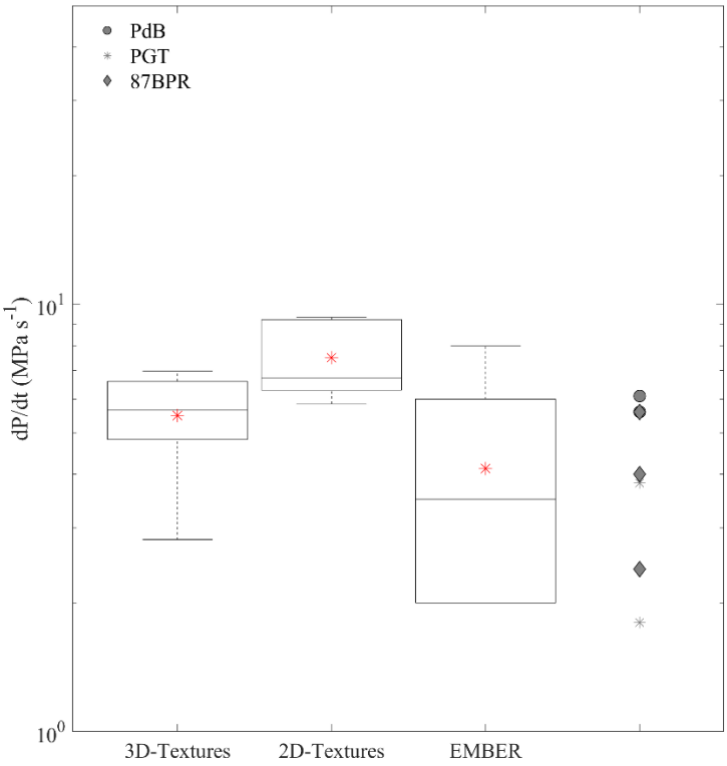

Figure 7: Box and whisker plots of decompression rates estimated by applying Shea (2017) models on 3D and 2D textural data, and the embayment diffusivity speedometer (EMBER). Whiskers indicate range limits, black horizontal lines medians, and red asterisks mean values. Previous data for explosive peralkaline magmas are included for comparison. PdB: Somma-Vesuvius Pomici di Base trachytic eruption (Pappalardo et al., 2018**); PGT: Pantelleria Green Tuff trachytic eruption (**Campagnola et al., 2016**); 87BPR: ~87 ka Baricha peralkaline rhyolitic eruption (**Tadesse et al., 2024**).**

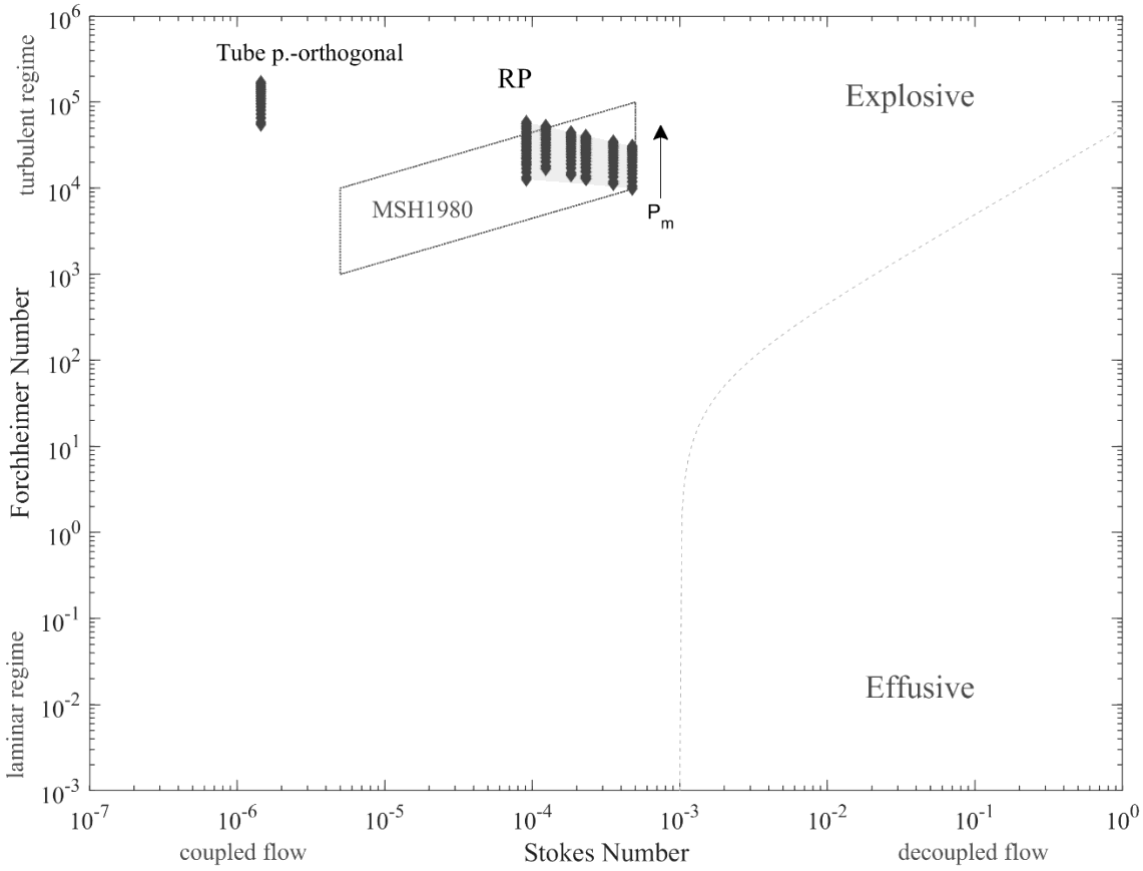

Figure 8: Stokes and Forchheimer numbers for the Rungwe Pumice (RP) samples represented as grey diamonds over a magmastatic pressure (Pm) range from 13 to 40 MPa (black arrow). The grey-shaded region represents the range for standard RP pumices, while values for the tube pumice across directions orthogonal to the main vesicle elongation are shown for comparison. Additionally, the range for the 1980 Mount St. Helens Plinian eruption (MSH1980; Degruyter et al., 2012**) is indicated (dotted contour). The dashed line marks the critical Stokes and Forchheimer numbers defining the transition between effusive and explosive regimes for MSH1980 rheology (**Degruyter et al., 2012**); although not directly applicable to RP, a variation of maximum one order of magnitude is expected (**Valdivia et al., 2022**).**

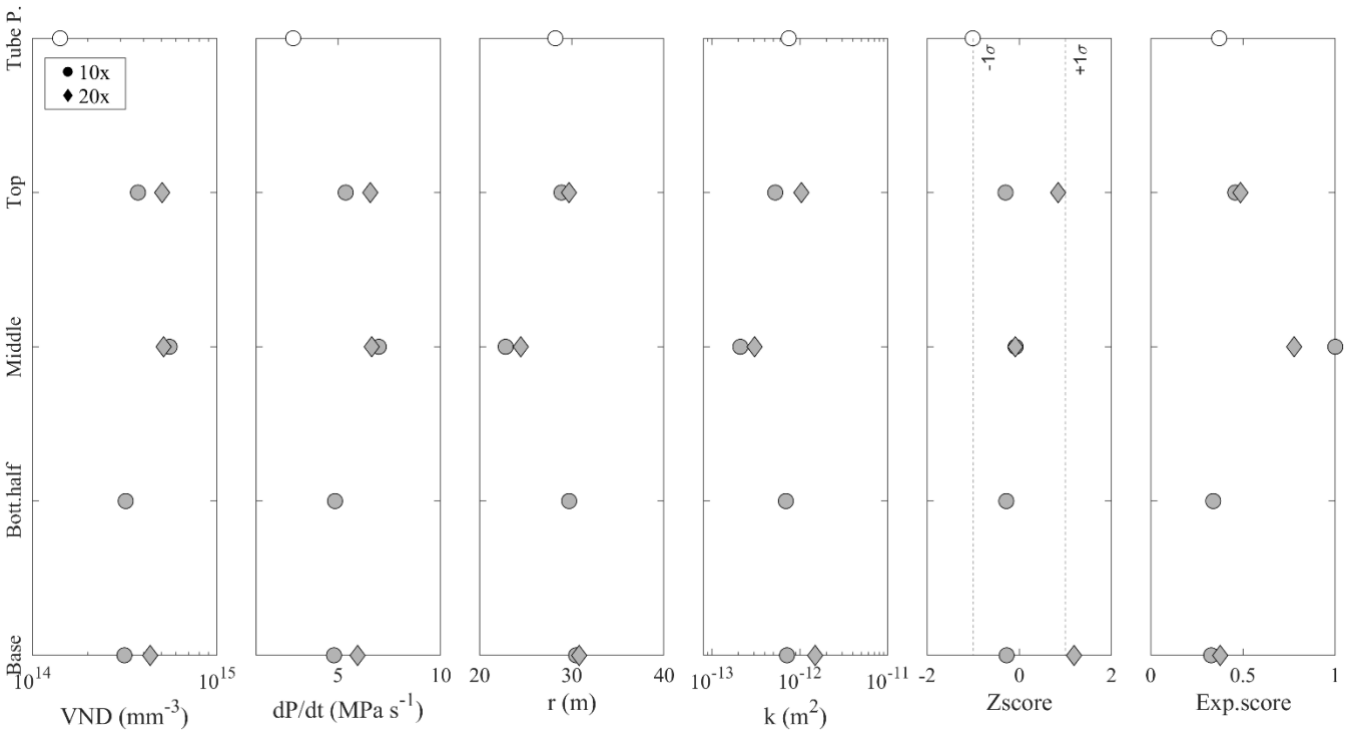

Figure 9: Comparison of key conduit parameters for different stratigraphic horizons analysed by µXCT: vesicle number density (VND), decompression rate (dP/dt), conduit radius (r), and Darcian permeability (k). An overall relative explosivity score—where 1 represents the maximum potential for explosivity—is calculated for each sample by summing the min-max normalised values of interdependent parameters promoting explosivity such as *dP/dt* and *k*. The reciprocal value of *k* was used in scoring, as it is inversely proportional to explosivity potential. Additionally, a normalised z score was calculated to express the interrelated consistency of these parameters.

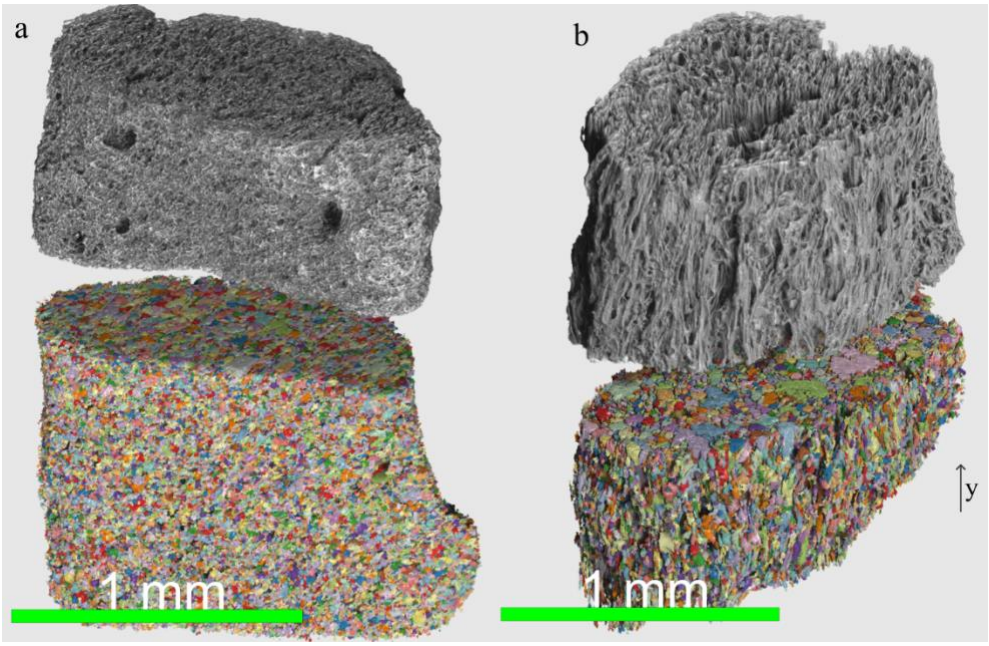

Figure 10: Grey-scale three-dimensional reconstructions and segmented vesicle volumes of a a) "standard" pumice and the b) tube pumice, providing a visual comparison of vesicle textures. In b) the y-axis indicates the direction of vesicle preferential orientation. Both particles were scanned with a 10x magnification lens.

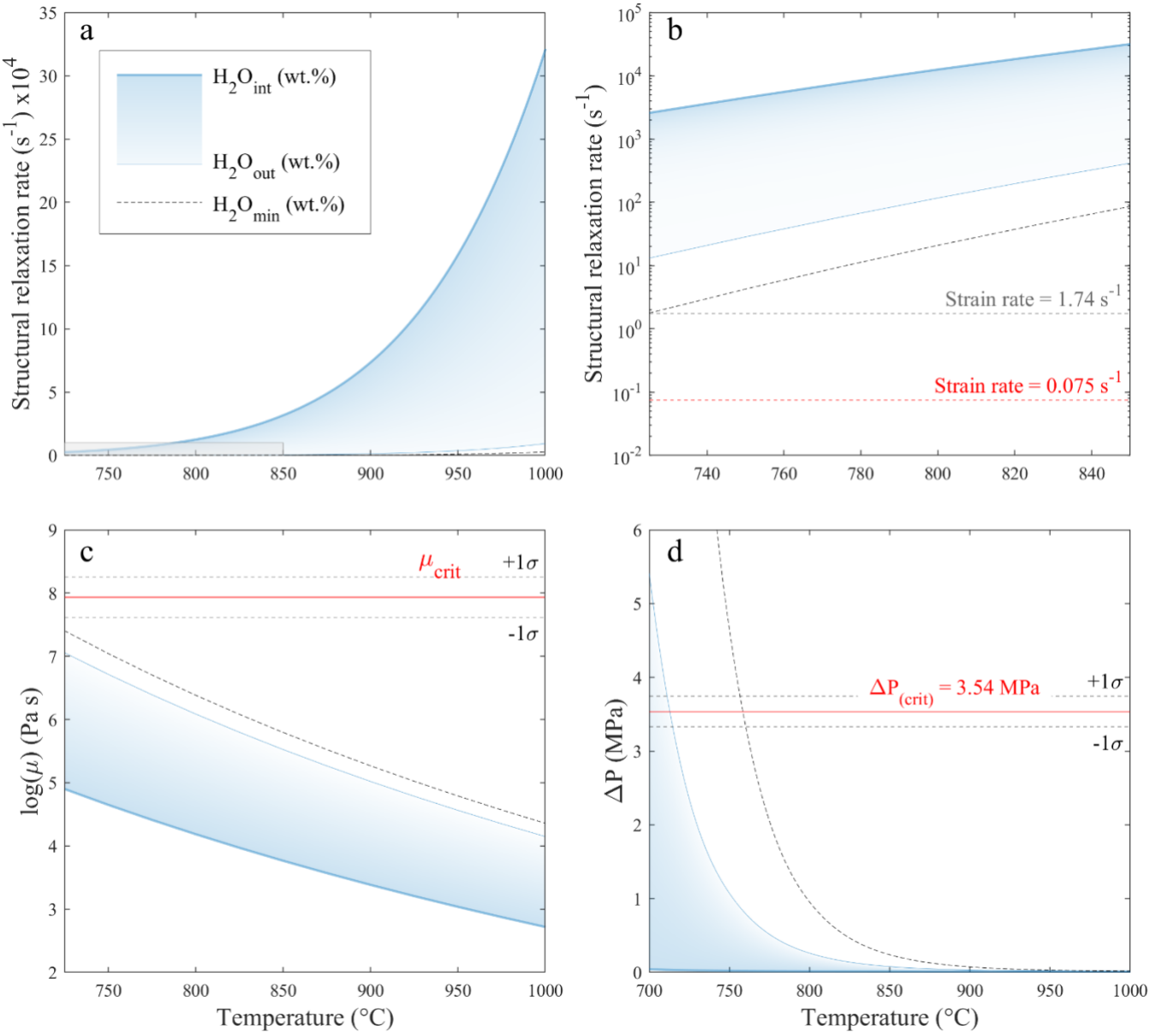

Figure 11: Different fragmentation criteria applied to the melt compositions of melt embayments spanning their water concentration range—from innermost (H_2O_{int}; thickest line) to outmost (H_2O_{out}; thinnest line) portions. The minimum water concentration inferred for a quenching pressure of 13 MPa (black dashed line) is also shown. The criteria have been evaluated for a range of temperatures (700-1000 °C) to represent the temperature drop due to the gas expansion upon ascent (see text for further details). Only one sample from the middle horizon is shown for clarity. a) Strain rate criterion is represented by melt structural relaxation drops caused by viscosity increase due to magma degassing and cooling. The grey inset highlights the close-up in the low-temperature region shown in b), where the criterion is satisfied when the critical strain rate (0.075 s^{-1}) exceeds the structural relaxation time. The hypothetical strain rate (1.74 s^{-1}) resulting from magma acceleration only within the last ~90 m of ascent is also shown; c) shear-induced fragmentation criterion expressed as viscosity increase, where fragmentation is expected when the viscosity (μ) exceeds the critical viscosity calculated for RP conditions (μ_{crit}). Average of μ_{crit} from the Monte Carlo simulation is indicated with a red line together with ±1σ (grey dashed lines); d) increase in bubble internal gas overpressure with increasing melt viscosity upon ascent where fragmentation is expected when the overpressure exceeds the average critical value of 3.54 MPa (red line with ±1σ indicated by grey dashed lines).

Tables

	3D Textures							2D Textures†		FOAM†
Sample	Lens	Envelope volume‡ (mm^3)	Vesicle number	VND (m^{-3})	Vesicularity	Connectivity	Surface Area per unit volume (mm^{-1})	Vesicularity *	VND** (m^{-3})	VND (m^{-3})
Top	10X	1.884	2.65×10^5	3.73×10^{14}	0.62	0.9986	145	0.76 ±0.05	$4.06 \pm 2.10 \times 10^{14}$	5.23×10^{14}
	20X	0.749	1.11×10^5	5.04×10^{14}	0.71	0.9999	160			
Top half								0.77 ±0.04	$4.92 \pm 3.60 \times 10^{14}$	4.91×10^{14}
Middle	10X	2.089	5.13×10^5	5.53×10^{14}	0.56	0.9993	182	0.72 ±0.08	$2.38 \pm 1.55 \times 10^{14}$	8.34×10^{14}
	20X	0.791	1.65×10^5	5.14×10^{14}	0.59	0.9997	188			
Bottom half	10X	2.312	2.79×10^5	3.21×10^{14}	0.62	0.9996	150	0.76 ±0.04	$3.61 \pm 2.38 \times 10^{14}$	8.53×10^{14}
Base	10X	2.227	2.54×10^5	3.15×10^{14}	0.64	0.9998	158	0.71 ±0.05	$3.84 \pm 3.00 \times 10^{14}$	4.24×10^{14}
	20X	0.914	1.14×10^5	4.35×10^{14}	0.71	0.9999	151			
Tube pumice	10X	2.155	1.36×10^5	1.42×10^{14}	0.56	0.9985	129			
Average‡				$4.31 \pm 8.95 \times 10^{14}$	0.64 ±0.05	0.9995 ±0.0004	162 ±15	0.74 ±0.06	$3.76 \pm 2.75 \times 10^{14}$	$6.25 \pm 1.81 \times 10^{14}$

‡ Volume of glass+vesicles. Open vesicles with an outlet diameter ≤70µm were closed by a wrapping surface; ‡ average of parameters for 3D datasets is calculated considering only "standard" pumices; † for each horizon, 2D Vesicularity and VND are given by the average of processed images for 10 different samples; *2D vesicularity is computed as fraction of vesicle area (excluding vesicles at borders) over total area (corrected for border vesicles); **2D VND is estimated from number per the unit area: Na/L where L is the average vesicle dimension, which can be written as $Na/\sqrt{(A/n)}$ with A: total vesicle area and n: number of vesicles; †2D VND stereologically corrected using FOAM.

1445 **Table 1. Vesicularity, VND, and geometric parameters of pumice textures analysed with 2D and 3D methods.**

Sample	Lens	VSD Slope (mm^{-1})	VSD n_0 (mm^{-3})	Average bubble growth rate ($mm \cdot s^{-1}$)	VVD equivalent diameter mode (μm)	Average sphericity
Top	10X	-95	5.46×10^5	6.81×10^{-4}	45	0.74 ±0.09
	20X	-93	5.71×10^5	6.94×10^{-4}	36	0.70 ±0.09
Middle	10X	-123	7.91×10^5	5.23×10^{-4}	36	0.74 ±0.10
	20X	-124	8.40×10^5	5.19×10^{-4}	36	0.70 ±0.10
Bottom half	10X	-94	4.95×10^5	6.88×10^{-4}	28	0.73 ±0.10
Base	10X	-82	3.65×10^5	7.90×10^{-4}	45	0.71 ±0.10
	20X	-87	6.44×10^5	7.45×10^{-4}	45	0.71 ±0.10
Tube pumice	10X	-68	1.66×10^5	9.55×10^{-4}	57	0.68 ±0.12
Average				7.22×10^{-4} ±1.37×10^{-4}	39 ±6*	

*Average VVD mode is calculated considering only "standard" pumices.

Table 2. Indicators derived from 3D size distribution trends and shape parameters. The slope and intercept of VSDs are provided, along with the estimated average growth rate.

	3D Textures				2D Textures†	Emb. Speedometer				
Sample	Lens	Decompression rate ($MPa \cdot s^{-1}$)	Ascent rate ($m \cdot s^{-1}$)	Conduit radius (m)	Decompression rate ($MPa \cdot s^{-1}$)	Sample	Decompression rate ($MPa \cdot s^{-1}$)	Final pressure (Mpa)	Final water concentration (wt.%)	Initial water concentration (wt.%)
Top	10X	5.4	199	28	6.7	Top	1.67	10	0.63	4
	20X	6.6	243	29		Top	2.78	10	0.63	5
Top half					6.5	Top	2.78	25	1.51	5
Middle	10X	7.0	259	23	9.2	Top half	2.78	5	0.32	4
	20X	6.6	246	24		Top half	0.56	15	0.93	5
Bottom half	10X	4.9	180	30	9.3	Top half	2.10	5	0.32	5
						Top half	0.20	15	0.93	3
Base	10X	4.8	178	30	5.9	Middle	0.80	15	0.93	4
	20X	5.9	220	31		Bottom half	2.00	20	1.22	4
Tube pumice	10X	2.8	104	36						
Average‡		5.9 ±0.9	218 ±30	28 ±3	7.5 ±1.5		1.74 ±0.95	13 ±6	0.82 ±0.37	4.3 ±0.7

	Outgassing parameters*									
		Darcian permeability (m^2)			Inertial permeability (m^2)			Stockes number		
Sample	Lens	x	y	z	x	y	z	x	y	z
Top	10X	4.84×10^{-13}	4.36×10^{-13}	6.56×10^{-13}	3.26×10^{-9}	2.83×10^{-9}	4.91×10^{-9}	6.38×10^{-5}	5.75×10^{-5}	8.65×10^{-5}
	20X	1.09×10^{-12}	8.77×10^{-13}	1.14×10^{-12}	9.76×10^{-9}	7.28×10^{-9}	1.04×10^{-8}	1.10×10^{-4}	8.83×10^{-5}	1.15×10^{-4}
Middle	10X	3.45×10^{-13}	1.27×10^{-13}	1.60×10^{-13}	2.06×10^{-9}	5.34×10^{-10}	7.28×10^{-10}	6.61×10^{-5}	2.44×10^{-5}	3.06×10^{-5}
	20X	2.53×10^{-13}	2.14×10^{-13}	4.55×10^{-13}	1.35×10^{-9}	1.08×10^{-9}	3.00×10^{-9}	4.14×10^{-5}	3.50×10^{-5}	7.46×10^{-5}
Bottom half	10X	6.35×10^{-13}	7.90×10^{-13}	6.57×10^{-13}	4.71×10^{-9}	6.32×10^{-9}	4.92×10^{-9}	7.94×10^{-5}	9.87×10^{-5}	8.21×10^{-5}
Base	10X	7.73×10^{-13}	6.41×10^{-13}	7.30×10^{-13}	6.13×10^{-9}	4.76×10^{-9}	5.68×10^{-9}	9.05×10^{-5}	7.50×10^{-5}	8.55×10^{-5}
	20X	1.57×10^{-12}	1.47×10^{-12}	1.42×10^{-12}	1.60×10^{-8}	1.46×10^{-8}	1.40×10^{-8}	1.44×10^{-4}	1.34×10^{-4}	1.30×10^{-4}
Tube pumice	10X	1.18×10^{-14}	7.49×10^{-13}	5.15×10^{-14}	2.15×10^{-11}	5.87×10^{-9}	1.57×10^{-10}	1.44×10^{-6}	9.13×10^{-5}	6.28×10^{-6}

‡Average of 3D datasets is calculated considering only "standard" pumices; † obtained from VND values corrected with stereological conversion in FOAM; *parameters estimated across three mutually orthogonal and randomly oriented directions.

Table3. Estimates of decompression rate calculated using both Shea (2017) equation for pumice textures and the embayment speedometer for comparison. Modelled fragmentation conditions and outgassing parameters are also reported.